HHS Public Access

Author manuscript

Cell Rep. Author manuscript; available in PMC 2022 June 01.

Published in final edited form as:

Cell Rep. 2022 May 03; 39(5): 110753. doi:10.1016/j.celrep.2022.110753.

Clearance of an amyloid-like translational repressor is governed by 14–3–3 proteins

S. Grace Herod[1,3], **Annie Dyatel**[1], **Stefanie Hodapp**[2], **Marko Jovanovic**[2], **Luke E. Berchowitz**[1,3,4,*]

[1]Department of Genetics and Development, Hammer Health Sciences Center, Columbia University Irving Medical Center, New York, NY, USA

[2]Department of Biological Sciences, Columbia University, New York, NY, USA

[3]Taub Institute for Research on Alzheimer's and the Aging Brain, New York, NY, USA

[4]Lead contact

SUMMARY

Amyloids are fibrous protein aggregates associated with age-related diseases. While these aggregates are typically described as irreversible and pathogenic, some cells use reversible amyloid-like structures that serve important functions. The RNA-binding protein Rim4 forms amyloid-like assemblies that are essential for translational control during *Saccharomyces cerevisiae* meiosis. Rim4 amyloid-like assemblies are disassembled in a phosphorylation-dependent manner at meiosis II onset. By investigating Rim4 clearance, we elucidate co-factors that mediate clearance of amyloid-like assemblies in a physiological setting. We demonstrate that yeast 14-3-3 proteins bind to Rim4 assemblies and facilitate their subsequent phosphorylation and timely clearance. Furthermore, distinct 14-3-3 proteins play non-redundant roles in facilitating phosphorylation and clearance of amyloid-like Rim4. Additionally, we find that 14-3-3 proteins contribute to global protein aggregate homeostasis. Based on the role of 14-3-3 proteins in aggregate homeostasis and their interactions with disease-associated assemblies, we propose that these proteins may protect against pathological protein aggregates.

In brief

Amyloids are protein aggregates associated with age-related diseases. Herod et al. demonstrate that yeast 14-3-3 proteins play critical roles in the clearance of functional amyloid-like assemblies.

*Correspondence: leb2210@cumc.columbia.edu.

AUTHOR CONTRIBUTIONS

S.G.H. and L.E.B. conceived of the study, designed the experiments, constructed strains, analyzed data, and wrote the paper. S.G.H. conducted the experimental procedures. A.D. assisted with experimental procedures. M.J. and S.H. conducted and analyzed mass spectrometry experiments and edited the manuscript.

DECLARATION OF INTERESTS

The authors declare no competing interests.

SUPPLEMENTAL INFORMATION

Supplemental information can be found online at https://doi.org/10.1016/j.celrep.2022.110753.

Additionally, 14-3-3 proteins contribute to global protein aggregate homeostasis. Based on these findings, they propose that 14-3-3 proteins may protect against pathological protein aggregates.

Graphical Abstract

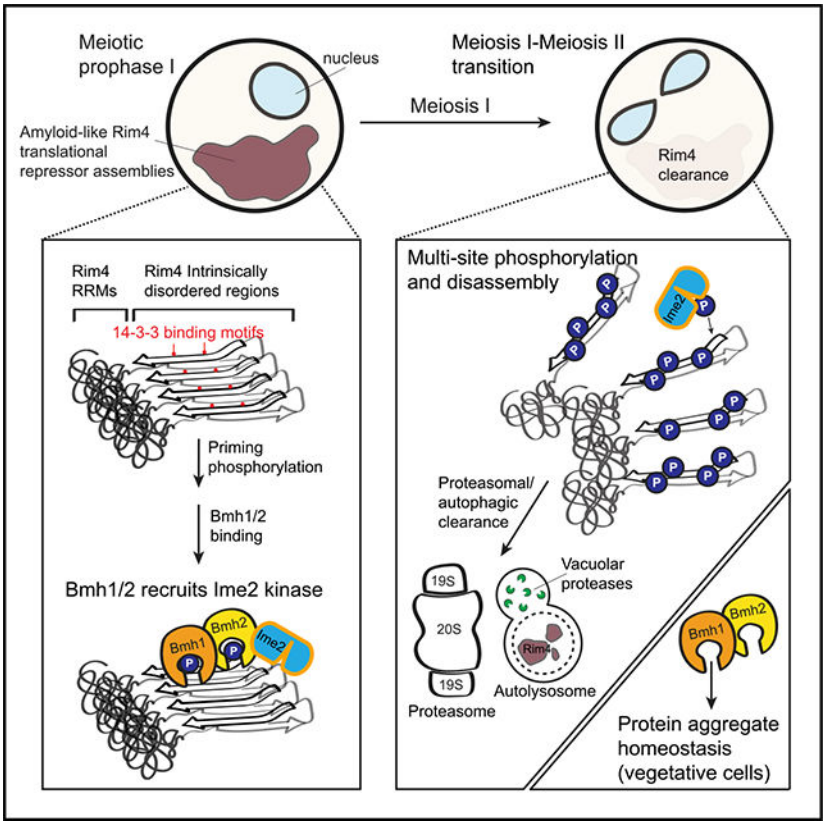

INTRODUCTION

Amyloids are fibrous protein aggregates that are associated with numerous age-related illnesses, including Alzheimer's disease, Parkinson's disease, and transthyretin amyloidosis (Knowles et al., 2014; Ruberg et al., 2019). These aggregates are typically described as irreversible and pathogenic. They exhibit specific properties, including resistance to ionic detergents and formation of stable cross-β-sheet structures (Liebman and Chernoff, 2012). Protein assemblies that share a subset of the biochemical properties associated with disease-related amyloids are termed amyloid-like (Newby and Lindquist, 2013). Amyloid aggregates often act in a dominant negative manner by sequestering monomeric proteins and rendering them inactive. In contrast, some amyloid-like assemblies can play functional roles in biological processes such as hormone storage and persistence of long-term memory (Khan et al., 2015; Maji et al., 2009). In budding yeast, the RNA-binding protein Rim4 forms functional and reversible amyloid-like assemblies that are essential for meiosis (Berchowitz et al., 2015). Understanding the reversibility of functional amyloid-like assemblies in physiological conditions could shed light on potential therapeutic approaches in disease-related amyloids.

Rim4 assemblies are translational repressors that operate exclusively during meiosis, which is a specialized type of cell division that generates haploid gametes from diploid progenitor cells. Cells undergoing meiosis perform two chromosomal divisions after a single replication event. The successful separation of homologous chromosome pairs during meiosis I requires the repression of gene products that drive sister-chromatid segregation during meiosis II (Carlile and Amon, 2008; Miller et al., 2012). Rim4 assemblies inhibit translation of mRNAs, such as the B-type cyclin *CLB3*, that encode protein products that are harmful when prematurely expressed, but are necessary for late meiotic events (Miller et al., 2012). When *CLB3* is mis-expressed before meiosis II, cells improperly segregate sister chromatids rather than homologous chromosome pairs at the first meiotic division, which can result in meiotic catastrophe and aneuploid gametes (Carlile and Amon, 2008; Miller et al., 2012). After meiosis I, Rim4 is hyperphosphorylated by the meiosis-specific kinase Ime2 and its amyloid-like properties are reversed. Rim4 monomers and oligomers are ultimately degraded by the proteasome and autophagy (Carpenter et al., 2018; Wang et al., 2020). Once cells have cleared Rim4 assemblies, previously repressed transcripts are now translated, allowing for late meiosis events such as meiosis II and spore formation (Berchowitz et al., 2013). Using Rim4 as a model, we sought to understand how phosphorylation contributes to clearance of amyloid-like assemblies.

Phosphorylation plays an important role in the etiology of several disease-related amyloids (Gong et al., 1993). For example, the Alzheimer's disease-associated protein tau is three to four times more phosphorylated in Alzheimer's disease brain issue than that of control brain tissue (Kopke et al., 1993). The phosphorylation of tau at specific sites disrupts its association with microtubules (Biernat et al., 1993), raising the question of whether phosphorylation is a driver of pathogenesis. However, whether and how phosphorylation directly contributes to the formation of pathological tau aggregates remains controversial owing to the large number of phosphorylation sites and their individual opposing contributions to tau's propensity for aggregation (Tenreiro et al., 2014). Hyperphosphorylated tau is also observed in physiological settings during early development when fetal brain cells are still dividing (Watanabe et al., 1993). Other examples of phosphorylated pathogenic aggregates include α-synuclein, which is frequently phosphorylated at S129 in the Lewy bodies found in patients with Parkinson's disease. While only approximately 4% of soluble α-synuclein is phosphorylated at this site, this proportion reaches approximately 90% within protein extracted from Lewy bodies (Fujiwara et al., 2002). However, whether this phosphorylation event is causative of disease is unclear. A better understanding of the direct contribution of phosphorylation to disease-associated aggregation is needed.

Many neurodegenerative disease-associated aggregates are bound by the phospho-binding 14-3-3 protein family. However, the pathological and/or protective nature of this association is unclear. 14-3-3 proteins typically bind to phosphorylated peptides and function as homo- or heterodimers. These proteins are involved in numerous pathways, including cell cycle checkpoints, apoptosis, and signal transduction (Ford et al., 1994; Gelperin et al., 1995; Steinacker et al., 2011). 14-3-3 proteins are abundant in the brain, representing 1% of the total soluble brain protein (Berg et al., 2003). These proteins seem to be important in neurodegenerative disease in that they are present in neurofibrillary tau tangles in

hippocampal samples from patients with Alzheimer's disease (Layfield et al., 1996). 14-3-3 proteins may also serve a protective role from Parkinson's disease-associated pathology. Some Parkinson's-associated mutations disrupt 14-3-3 binding to α-synuclein, parkin, and LRRK2, suggesting that these interactions are important for neuronal physiology (Foote and Zhou, 2012).

Here, we show that Rim4 amyloid-like assemblies interact with the budding yeast 14-3-3 proteins, Bmh1 and Bmh2. We demonstrate that the interaction between Rim4 and 14-3-3 proteins is critical for timely disassembly and clearance of Rim4. 14-3-3 proteins facilitate the phosphorylation of Rim4 by its kinase, Ime2, thus contributing to Rim4 disassembly and degradation. Our results support a model by which Bmh1 and Bmh2 play non-redundant roles in facilitating the phosphorylation of amyloid-like Rim4. By dissecting the basis of how 14-3-3 proteins contribute to the clearance of amyloid-like Rim4 assemblies, our results provide a mechanistic model describing how 14-3-3 proteins may interact with phosphorylated residues to regulate and protect against disease-associated protein aggregates.

RESULTS

Rim4 assemblies are associated with 14–3–3 proteins Bmh1 and Bmh2

During meiosis, Rim4 assembles into functional amyloid-like translational repressors that are reversed and cleared at meiosis II onset (Figure 1A) (Berchowitz et al., 2015; Carpenter et al., 2018). To determine the co-factors that are important for Rim4 clearance and/or assembly, we used a biochemical strategy designed to identify proteins that bind specifically to the assembled form of Rim4. Rim4 contains three RNA-recognition motifs, two intrinsically disordered regions (IDRs), and a C-terminal prion-like domain (Alberti et al., 2009; Berchowitz et al., 2015; Soushko and Mitchell, 2000). The Rim4 C-terminal IDR is required for assembly and translational control (Berchowitz et al., 2015). We immunopurified (IPed) full-length Rim4 and Rim4DIDR from G2-arrested meiotic yeast cells. We then analyzed Rim4-bound proteins by quantitative mass spectrometry. Two of the most highly enriched proteins were Bmh1 and Bmh2, the two 14-3-3 proteins in *Saccharomyces cerevisiae (S. cerevisiae).* (Figure 1B). Importantly, we found that the association between Rim4 and 14-3-3 proteins is vastly more enriched in full-length Rim4 IPs compared with Rim4DIDR IPs. These data are consistent with the model that 14-3-3 proteins associate preferentially with full-length, assembled Rim4.

To validate the interaction between Rim4 and 14-3-3 proteins and to evaluate the timing during meiosis when this interaction occurs, we performed a reciprocal co-IP of 14-3-3 proteins in cells synchronously progressing through meiosis. To induce synchronous meiosis, we used an *NDT80* block-release system (Benjamin et al., 2003), *NDT80-IN*. The *NDT80-IN* system enables control of the expression of Ndt80, which is the transcription factor responsible for exit from meiotic G2 and entry into the meiotic divisions. *NDT80-IN* cells in sporulation medium will enter meiosis, but arrest in meiotic G2, and will progress synchronously through meiotic divisions only upon induction of *NDT80* transcription. We found that Rim4 co-purified with both Bmh1 and Bmh2 in early meiosis as well as during meiosis I and II (Figures 1C and 1D).

14–3–3 proteins are important for clearance of assembled Rim4 in meiosis II

To investigate a possible role for Bmh1 and/or Bmh2 in Rim4 clearance, we analyzed whether deletion of either *BMH1* or *BMH2* would cause meiotic cells to aberrantly retain Rim4 in meiosis. While the *bmh1*Δ *bmh2*Δ double mutant is inviable in many *S. cerevisiae* laboratory strains (Van Heusden et al., 1995) (Figure S1A), *bmh1*Δ and *bmh2*Δ single mutants are largely dispensable for mitotic growth in all media we tested (Figure S1B). In contrast, *bmh1*Δ and *bmh2*Δ single mutants display meiotic progression delays (Figure S2A), supporting a potential role for Bmh1 and Bmh2 in Rim4 biology. To assess the assembly state of Rim4 throughout meiosis, we used semi-denaturing detergent agarose gel electrophoresis (SDD-AGE). SDD-AGE tests for the presence of SDS-resistant assemblies, which are a hallmark of amyloid-like complexes, such as those formed by yeast prions (Kryndushkin et al., 2003). We found that both *bmh1*Δ and *bmh2*Δ mutants exhibit delayed clearance of SDS-resistant Rim4 assemblies (Figure 2A). As expected, we found that both *bmh1*Δ and *bmh2*Δ show persistent Rim4 protein via SDS-PAGE, which tests for the presence of the protein, regardless of its assembly state (Figures 2B and S2B). A key characteristic of mutants that fail to clear Rim4 at the meiosis I-meiosis II transition is the inability to de-repress the translation of Rim4 mRNA targets such as *CLB3* (Berchowitz et al., 2013). We found that both *bmh1*Δ and *bmh2*Δ show delayed translation of Clb3 protein (Figures 2C and S2B). Together these results are consistent with the idea that 14-3-3 mutants are defective for Rim4 clearance.

The delay in disassembly and clearance of Rim4 could be due to the meiotic progression delays we observe in *bmh* mutants (Figure S2A). To address this issue, we used single-cell immunofluorescence to analyze Rim4 abundance at specific stages throughout meiosis. We found that Rim4 aberrantly persists in metaphase II and anaphase II in both *bmh1*Δ and *bmh2*Δ mutants, indicating that the Rim4 persistence defect is not an artifact of delayed meiosis (Figures 2D and 2E). Our results suggest that 14-3-3 proteins are important for the timely clearance and possibly disassembly of Rim4 during meiosis II, and that 14-3-3 proteins play an important role in coupling Rim4 clearance to meiotic progression.

Bmh1 and Bmh2 play distinct roles in Rim4 clearance

Bmh1 and Bmh2 sequences have a high percent identity and are sometimes referred to as redundant. Indeed, cells lacking either protein grow normally during mitosis (Figure S1B). Their main sequence divergence is at the C-terminus; they share 98% identity within the first 242 amino acids, but only 58% identity within the C-terminal 25–31 amino acids (Figure 3A). Bmh1 and Bmh2 preferentially form heterodimers, although homodimers are also present (Chaudhri et al., 2003). This suggests that Bmh1/Bmh2 heterodimers perform housekeeping functions, while their respective homodimers perform more specialized roles. Bmh1 is the major isoform and is expressed approximately 3.4 times more than Bmh2 during vegetative growth (Slubowski et al., 2014). However, the expression levels become more balanced in meiosis, with Bmh1 expressed approximately 1.7-fold higher than Bmh2 (Slubowski et al., 2014). To assess whether Bmh1 and Bmh2 act non-redundantly, we generated strains with cells expressing *BMH1* from both 14-3-3 loci, called *2xBMH1* and cells expressing *BMH2* from both loci, called *2xBMH2* (Figure 3B). These cells maintain

the original promoters and terminators, and express equivalent levels of total 14-3-3 protein compared with wild type (Figures S3A–S3D).

We first assessed whether *2xBMH1* and *2xBMH2* cells properly clear Rim4 assemblies at meiosis II onset. Both *2xBMH1* and *2xBMH2* cells showed delayed disassembly of amyloid-like Rim4 in SDD-AGE assays (Figure 3C). However, we note that the loading in *2xBMH2* is increased at later time points, which could partially explain the increased signal. As expected, we observed that both *2xBMH1* and *2xBMH2* cells exhibit delayed clearance of total Rim4 by SDS-PAGE (Figures 3D and S3E). Both mutant strains also have delayed maximal translation of Clb3 protein (Figures 3E and S3E), consistent with the idea that each 14-3-3 isoform is distinctly important for the timely disassembly of the repressor form of Rim4. We note that Clb3 protein does begin to become translated slightly earlier in *2xBMH1* cells, which could reflect either premature disassembly or defective Rim4 in this mutant. To address this concern, we measured Rim4 signal at specific stages throughout meiosis. We found that, in both *2xBMH1* and *2xBMH2* cells, Rim4 protein aberrantly persisted in metaphase II and anaphase II cells (Figures 3F and 3G). Together, these results support the hypothesis that Bmh1 and Bmh2 function non-redundantly to couple Rim4 clearance with meiotic progression.

14–3–3 protein interaction with Rim4 requires priming phosphorylation within its IDR

We next wanted to determine which part of Rim4 interacts with Bmh1 and Bmh2. Rim4 clearance depends on multi-site phosphorylation within its C-terminal IDR (Carpenter et al., 2018). Because 14-3-3 proteins generally bind phosphorylated peptides, we assessed the interactions between Bmh proteins and Rim4 phospho-mutants by co-immunoprecipitation (co-IP). We tested a Rim4 phospho-mutant allele in which 47 serine and threonine residues within the C-terminal IDR were mutated to alanine (*RIM4-47A*, from T450 onward) to prevent phosphorylation at these sites (Figure S4A). We previously found that this region is extensively phosphorylated during meiosis and that phospho-mutants within this region are defective for Rim4 clearance (Carpenter et al., 2018). We found that neither Bmh protein associates with Rim4-47A (Figures S4B and S4C) and that Rim4-47A could not be disassembled (Figure S4D). This supports the idea that Bmh1 and Bmh2 interact with previously phosphorylated residues in the IDR, which are essential for subsequent Rim4 disassembly.

Furthermore, we tested sub-combinations of these 47 serine and threonine substitutions: the 10 most distal sites (*RIM4-10A*), the 27 most distal sites (*RIM4-27A*), and the 21 most proximal sites (*RIM4-21A*) (Figure S4A). Rim4-10A maintains the interaction with both Bmh1 and Bmh2 (Figures S4B and S4C), and the *RIM4-10A* mutation has no effect on Rim4 assembly clearance (Figure S4D). Thus, the 10 most distal serine/threonine residues of the C-terminal IDR are dispensable for both Rim4-Bmh interaction and Rim4 disassembly and clearance. Rim4-27A encompasses the 10 substitution sites of Rim4-10A. Like Rim4-10A, Rim4-27A maintains the interaction with Bmh1 and Bmh2 (Figures S4B and S4C). Unlike the *Rim4-10A* mutant, *RIM4-27A* exhibits a disassembly defect, though milder than that of *RIM4-47A* (Figure S4D). Rim4-21A and Rim4-27A share only one substitution site. However, while *RIM4-21A* mutants exhibit a disassembly defect similar to

RIM4-27A (Figure S4D), Rim4-21A does not interact with either Bmh1 or Bmh2 (Figures S4B and S4C), reminiscent of Rim4-47A. Thus, we conclude that the primary interaction between Bmh proteins and Rim4 likely resides within the 20 most proximal phosphorylation sites studied.

We next wanted to assess the effect on Rim4 clearance when the interaction between Rim4 and Bmh proteins is abrogated. We found that both *RIM4-21A* and *RIM4-47A*, which do not interact with either Bmh1 or Bmh2, aberrantly maintain Rim4 protein in meiosis II (Figure S4E). Unexpectedly, *RIM4-27A* mutants, which preserve the 14-3-3 protein interaction, also maintain Rim4 in meiosis II (Figure S4E). Wild-type and *RIM4-10A* mutants did not show persistent Rim4 in meiosis II (Figure S4E). This suggests that the interaction between Bmh proteins and Rim4 is necessary but not sufficient for proper Rim4 clearance.

There are two 14-3-3 binding motifs within the Rim4 C-terminal IDR (Madeira et al., 2015). One occurs at S525, which is within the Rim4-21A mutated region. The second 14-3-3 binding motif is at S612, which is within the Rim4-27A mutated region (Figure 4A). Because 14-3-3 proteins function as homo- and heterodimers, the dimer has two substrate binding regions. On many 14-3-3 substrates, there is a preferred binding site that facilitates binding on weaker secondary sites. The preferred site functions as a gatekeeper, and, in the absence of phosphorylation at this site, the secondary sites are too weak to facilitate binding (Yaffe, 2002). To assess whether these 14-3-3 binding sites are important for the interaction between Rim4 and Bmh1/2 proteins, we generated strains in which Rim4 had both S525 and S612 mutated to alanine. The interaction between Bmh1/2 and Rim4-S525A-S612A is greatly decreased (Figures 4B and 4C), supporting our hypothesis that the phosphorylation of these two amino acids is important for the interaction. We next wanted to test whether these mutations affect Rim4 assembly and clearance. We found that Rim4-S525A-S612A strains have delayed clearance of Rim4 assemblies and have persistent Rim4 in meiosis II (Figures 4D and 4E). Furthermore, we found that Rim4-S525A-S612A mutants display an electrophoretic band shift on SDS-PAGE (Figure 4F). The band shift is enhanced when the samples are run on a phos-tag gel, which slows the migration of phosphorylated proteins (Figure 4F), suggesting the band shift represents changes in Rim4 phosphorylation status. A band shift that is visible on an SDS-PAGE gel is unlikely to be the result of two phosphorylation events. Rather, our data suggest that mutating S525 and S612 affects phosphorylation of additional, downstream sites on Rim4. Based on our data, we propose that Bmh proteins interact with the Rim4 C-terminal IDR in a manner that requires a priming phosphorylation event at S525. However, other 14-3-3 binding sites within the Rim4-27A region, such as S612, contribute to timely Rim4 clearance.

14–3–3 proteins interact with Ime2st

In mammalian Alzheimer's disease models, 14-3-3 proteins link several kinases to tau, resulting in its hyperphosphorylation (Agarwal-Mawal et al., 2003; Hashiguchi et al., 2000; Li and Paudel, 2007). We hypothesized that yeast 14-3-3 proteins could be playing a similar role with Rim4. Rim4 is directly phosphorylated by Ime2 kinase at meiosis II onset (Berchowitz et al., 2013), which drives the disassembly and clearance of amyloid-like Rim4 (Carpenter et al., 2018). To investigate the idea that Bmh proteins act as the linker

between Rim4 and Ime2, we performed co-IP assays in which we purified Bmh1 and Bmh2 from meiotic cells and assessed Ime2 association. We could not detect co-purification of Ime2 with either Bmh1 or Bmh2 (Figures S5A and S5B). Because the interactions between kinases and substrates are often transitory, we optimized our chances of detecting an interaction by using cells expressing a stable, hyperactive isoform of Ime2 (termed Ime2st) (Sia and Mitchell, 1995). Furthermore, we conducted our assays in G2-arrested cells in which Ime2st is highly active while Rim4 clearance is inhibited. In these conditions, we found that both Bmh1 and Bmh2 co-purify with Ime2st, with the association increasing with time in the G2 arrest (Figures 5A and 5B). These data are consistent with the model that 14-3-3 proteins link Ime2 kinase to its substrate, Rim4.

14–3–3 proteins are critical for interaction between Ime2 and Rim4 assemblies

We next tested whether 14-3-3 proteins are important for the interaction of Ime2 with assembled Rim4. Because Rim4 assemblies migrate as SDS-resistant particles in SDD-AGE assays, we asked whether Ime2 co-migrates with high-molecular weight Rim4 assemblies. Ime2 signal at the high molecular weight (>250 kDa) range of the gel is indicative of assembly association, whereas Ime2 signal at low molecular weight (approximately 50 kDa) range indicates monomeric protein. Compared with *bmh1*Δ or *bmh2*Δ mutants, we found that wild-type cells contain a larger proportion of assembly-associated Ime2 protein versus monomers in early meiosis (Figure 5C). We also assessed Ime2 association with SDS-resistant assemblies in strains in which both Bmh1 and Bmh2 are hypomorphic. Bmh1 and Bmh2 were rendered hypomorphic by C-terminally tagging with an auxin-inducible degron (AID) sequence (Morawska and Ulrich, 2013). Even in the absence of auxin, strains containing both Bmh1-AID and Bmh2-AID did not enter meiotic divisions (Figure S5C). From this, we concluded that the AID tags themselves render Bmh1 and Bmh2 hypomorphic. Ime2 association with SDS-resistant assemblies was almost entirely prevented in Bmh1/2 hypomorphs (Figure 5C). We could not assess whether SDS-resistant Ime2 requires assembled Rim4 because *rim4*Δ*IDR* mutants do not express Ime2. This is likely because expression of *IME2* depends on Rim4 (Deng and Saunders, 2001), and Rim4ΔIDR may either be too unstable or functionally unable to induce *IME2* expression. The absence of assembly-associated Ime2 in *bmh1* and *bmh2* double hypomorphs suggests that 14-3-3 proteins are essential for this association. As meiosis progresses, the proportion of Ime2 associated with assemblies becomes similar in *bmh1*Δ and *bmh2*Δ mutants compared with wild type. This demonstrates that, in the absence of either Bmh1 or Bmh2, Ime2 association with assemblies is delayed.

We next wanted to test whether *bmh1*Δ or *bmh2*Δ mutants could delay the association between hyperactive Ime2 (Ime2st) and Rim4 assemblies using SDD-AGE assays. We found that monomeric Ime2st is only present in *bmh1*Δ and *bmh2*Δ mutants and not in wild-type cells (Figure S5D), supporting the idea that Bmh proteins assist Ime2 association with SDS-resistant assemblies. Our data are consistent with the model that Bmh proteins are important for the association of Ime2 with Rim4 assemblies.

14–3–3 proteins facilitate phosphorylation of Rim4 by Ime2 kinase

Because Bmh proteins are important for the interaction between Rim4 and Ime2, we next investigated whether Bmh proteins are important for phosphorylation of Rim4 by Ime2. We first examined whether *bmh* mutants suppress the dominant phenotypes associated the hyperactive *IME2*st allelic variant. *IME2*st mutants prematurely hyperphosphorylate Rim4, triggering aberrant disassembly (Carpenter et al., 2018) and de-repression of translation of Rim4 target transcripts, such as *CLB3* (Figures 6A and S6). Consistent with the model that Bmh proteins link Rim4 and Ime2 kinase, we found that, in *IME2*st*; bmh1*Δ double mutants, the *IME2*st-dependent premature translation of *CLB3* phenotype is suppressed. Clb3 protein is still expressed early in these mutants, but at lower levels than in the *IME2*st mutants alone.

To test this model directly, we assessed whether *bmh* mutants alter Rim4 phosphorylation status in an *IME2*st background. *IME2*st mutants exhibit highly phosphorylated Rim4, which can be visualized as an electrophoretic band shift using SDS-PAGE. We used this band shift readout to assess whether *bmh* mutants affect Rim4 phosphorylation. We found that, in *bmh* mutants, Rim4 remains in an unphosphorylated state, which is maintained late in meiosis. The aberrant persistence of unphosphorylated Rim4 can be clearly visualized on a phos-tag gel (Figure 6B). These data are consistent with the idea that Ime2st associated with Rim4 assemblies in *bmh1*Δ or *bmh2*Δ backgrounds cannot properly phosphorylate Rim4, despite maintaining an interaction (Figure S5D).

To further assess whether Bmh proteins facilitate the phosphorylation of assembled Rim4, we reconstituted the kinase reaction *in vitro*. We added purified Bmh1, Bmh2, both, or neither to a reaction containing both assembled Rim4 and Ime2st. BSA was used as a control for molecular crowding in reactions lacking one or both Bmh proteins. We assayed incorporation of radiolabeled phosphate and found that the addition of either Bmh1 or Bmh2 increased the phosphorylation of Rim4 (Figures 6C, 6D and S7). Addition of both Bmh1 and Bmh2 slightly increased phosphorylation of Rim4 more than the addition of either 14-3-3 protein individually. We also noticed that addition of Bmh1 and/or Bmh2 increased Ime2st autophosphorylation over the course of the assay. Autophosphorylation of Ime2 is a mechanism of Ime2 activation that is essential for meiotic progression (Schindler and Winter, 2006; Sopko et al., 2002). This suggests that 14-3-3 proteins may have additional roles in the Ime2 kinase cascade. These data are consistent with the model that 14-3-3 proteins facilitate the phosphorylation of Rim4 by Ime2 and contribute to the timely clearance of amyloid-like Rim4.

14–3–3 proteins are important for maintaining protein aggregate homeostasis

We next wanted to understand if 14-3-3 proteins play a general role in the homeostasis of protein aggregates beyond Rim4. To assess protein aggregate burden, we used a reporter strain containing Hsp104-mCherry. Hsp104 foci are indicative of the presence of protein aggregates, including those often associated with amyloid-like prion assemblies (Narayanan et al., 2006; Shorter and Lindquist, 2006). Hsp104 is a member of the conserved Hsp100 disaggregase family, which is essential for survival during various environmental stressors (Sanchez and Lindquist, 1990; Sanchez et al., 1992). Hsp104 interacts with the Sup35 yeast prion assemblies found in the [*PSI*+] background, breaking the aggregates up into smaller

seeds that are essential for prion propagation (Chernoff et al., 1995; Glover and Lindquist, 1998).

We found that the vast majority of mitotic wild-type cells do not contain Hsp104 foci. In contrast, *bmh1*Δ and *BMH1/2-AID* (hypomorphic), but not *bmh2*Δ, mutants exhibit a significantly higher percentage of cells that contain Hsp104-mCherry foci compared to wild type (Figures 7A and 7B). In addition, the cells that do contain Hsp104 foci in *bmh1*Δ and *BMH1/2*-hypomorphs contain larger numbers of foci per cell (Figure 7C). While our steady-state measurements cannot differentiate between whether Bmh proteins affect aggregate formation and/or clearance, these data support a model in which 14-3-3 proteins play an important role in general aggregate homeostasis.

DISCUSSION

Here, we demonstrate that the timely disassembly and clearance of amyloid-like Rim4 assemblies requires the two yeast 14-3-3 proteins, Bmh1 and Bmh2. The interaction between Rim4 and 14-3-3 proteins depends on a priming phosphorylation event within the Rim4 C-terminal IDR. We find that 14-3-3 proteins facilitate Rim4 phosphorylation via Ime2, thus enabling the events required for Rim4 clearance. Furthermore, we demonstrate that, during meiosis, Bmh1 and Bmh2 play non-redundant roles in facilitating Rim4 clearance. Beyond Rim4, we find that *bmh* mutants exhibit significant increases in protein aggregate burden, suggesting that 14-3-3 proteins are generally important for maintaining protein homeostasis.

14–3–3 proteins facilitate Rim4 phosphorylation

We generated several lines of evidence consistent with the notion that 14-3-3 proteins facilitate Rim4 phosphorylation by Ime2. First, Rim4 persists in its non-hyperphosphorylated state in *bmh1*Δ*; IME2*st and *bmh2*Δ*; IME2*st double mutants. In contrast, in the *IME2*st background alone, all Rim4 protein is hyperphosphorylated and cleared prematurely. The *bmh1*Δ and *bmh2*Δ mutants also suppress the dominant phenotypes associated with *IME*^{2st} mutants, including premature derepression of translation of Rim4 target transcripts. Furthermore, Ime2 associates with SDS-resistant assemblies in wild-type strains, but *bmh1*Δ and *bmh2*Δ mutants accumulate more monomeric Ime2. *BMH1/2* double hypomorphs significantly impair Ime2 association with SDS-resistant assemblies. This supports the idea that Ime2 depends on Bmh proteins for its interaction with Rim4 amyloid-like assemblies. Finally, 14-3-3 proteins interact with Ime^{2st}. An interaction between 14-3-3 proteins and another meiotic kinase, Sps1, has been demonstrated to be important for spore formation (Slubowski et al., 2014). These results highlight that meiotic cells rely on interactions between 14-3-3 proteins and regulatory kinases to ensure proper development. Developmentally regulated clearance of Rim4 is similar to disease-associated tau assemblies in that 14-3-3 proteins link tau to various kinases, facilitating its phosphorylation (Agarwal-Mawal et al., 2003; Hashiguchi et al., 2000; Yuan et al., 2004).

While our data support a role for Bmh proteins in establishing Rim4 phosphorylation, these proteins may act at other stages of the Rim4 clearance mechanism. A second potential role

for Bmh proteins in Rim4 clearance is as a chaperone to disassemble Rim4 monomers from the amyloid-like assembly. One idea termed the molecular anvil hypothesis posits that 14-3-3 proteins can function as chaperones owing to their highly stable dimer conformation (Yaffe, 2002). Each monomer contains a ligand-binding domain and nine α-helices. Strong interactions between the α-helices result in negligible movement between bound and unbound 14-3-3 dimers (Obsil et al., 2001; Rittinger et al., 1999; Yaffe, 2002), suggesting that Bmh dimers could bind to multiple phospho-sites on Rim4 and alter its conformation. While this is an attractive theory, the stronger association between Bmh proteins and Rim4 in early meiosis suggests that these proteins act earlier in the Rim4 clearance process than the disassembly step. It is also possible that hyperphosphorylation alone is sufficient to disassemble Rim4 amyloid-like assemblies owing to electrostatic repulsion (Monahan et al., 2017). Our future studies will be aimed at gaining a structural understanding of the Rim4 disassembly process by testing whether phosphorylation and Bmh proteins have the ability to alter Rim4 folding.

Another potential role for Bmh proteins is in the degradation process, where they may shuttle Rim4 monomers to the proteasome and/or autophagic machinery. This would be reminiscent of previous studies showing that 14-3-3 proteins target misfolded proteins to aggresomes by recruiting chaperone-associated proteins to dynein motors (Xu et al., 2013). Aggresomes are large juxtanuclear inclusion bodies that alleviate the toxicity of aggregates and facilitate their clearance by the recruitment of chaperones, proteasomes, and autophagic machinery (Garcia-Mata et al., 2002; Lee et al., 2002). Additional studies are necessary to determine the contribution of 14-3-3 proteins to the clearance of monomeric Rim4 and other aggregation-prone proteins.

14–3–3 proteins may protect against neurodegenerative disease

Amyloid assemblies are often associated with age-associated diseases. The role of phosphorylation in disease-associated amyloids is complex. Tau protein has a paperclip conformation that can loosen or tighten based on phosphomimetic mutations. S199E + S202E + T205E tau mutations loosen the paperclip conformation, as do S396E + S404E mutations (Jeganathan et al., 2008). However, when these mutations are combined, the paperclip conformation tightens. Tau has numerous phosphorylation sites and the contributions of these sites to tau's propensity for aggregation vary. Furthermore, 14-3-3 proteins have been shown to promote aggregation of non-phosphorylated tau, but this aggregation is prevented in phosphorylated tau (Hernández et al., 2004). Once tau is already aggregated, it can become phosphorylated by PHF kinase, which could contribute to the finding that aggregated tau in neurological disease is highly phosphorylated (Jicha et al., 1999).

Notably, 14-3-3 proteins interact with the aggregated forms of several other disease-associated proteins, including α-synuclein and could protect against disease phenotypes (Foote and Zhou, 2012). In mouse neuronal cell lines, 14-3-3theta overexpression decreases α-synuclein oligomerization, seeding capacity, and toxicity, whereas 14-3-3theta inhibition increases these metrics (Wang et al., 2018). Similarly, 14-3-3theta transgene overexpression in mouse brain regions delays α-synuclein aggregation *in vivo* and rescues behavioral

deficits associated with α-synuclein fibrils (Underwood et al., 2021). Additionally, 14-3-3 proteins interact with perinuclear inclusion bodies of huntingtin protein (Waelter et al., 2001). In yeast, Bmh1 is critical for targeting exogenously expressed mutant huntingtin to aggresomes (Wang et al., 2009), further suggesting a protective role for 14-3-3 proteins. We propose that, rather than a causative event, phosphorylation of aggregation-prone proteins may be secondary to aggregation and may be part of an anti-aggregation response that is mediated by 14-3-3 proteins.

In the case of spinocerebellar ataxia type I (SCA1), 14-3-3 proteins can exacerbate neurodegenerative disease phenotypes. SCA1 is caused by an expansion of a glutamine tract in the ataxin-1 protein (Zoghbi and Orr, 1995). 14-3-3 proteins bind to phosphorylated mutant ataxin-1 and slow its degradation (Chen et al., 2003). A decrease in 14-3-3 levels in mice with mutant ataxin-1 partially rescues the SCA1 phenotype, suggesting a role for 14-3-3 proteins in the disease (Jafa-Nejad et al., 2011). However, the detrimental effect of 14-3-3 proteins on neurotoxicity relies on mutant ataxin-1. The interaction between Rim4 and Bmh proteins, in contrast, is physiological, and in this case 14-3-3 proteins positively regulate disassembly of amyloid-like Rim4. Recent work suggests that 14-3-3 proteins may actually play a neuroprotective role in the case of mutant ataxin-1. 14-3-3 proteins have the capacity to act as chaperones for mutant ataxin-1, thus preventing its self-assembly and maintaining it in a soluble state in the cytosol (Leysen et al., 2021). With the advancement of small molecule stabilizers of 14-3-3/client interactions (Kaplan et al., 2017), the possibility of pharmacological targeting of 14-3-3 proteins could become therapeutically useful for several neurodegenerative diseases.

Bmh1 and Bmh2 play different roles in Rim4 biology

Because the two yeast 14-3-3 isoforms have a high percentage of similarity and typically form dimers with other isoforms without restriction, it is difficult to synthesize a model where individual isoforms perform distinct functions. However, specific 14-3-3 isoforms can play non-redundant roles such as 14-3-3 sigma, which preferentially forms homo-dimers to promote cap-dependent translation in mammalian cells (Chan et al., 1999; Wilker et al., 2007). Our data demonstrate that Bmh1 and Bmh2 are each individually important for the timely clearance of Rim4 during meiosis II. While Bmh1 and Bmh2 are highly similar, they do have variant C-termini with notable features. Bmh1 harbors a stretch of 10 consecutive glutamines at the C terminus, and Bmh2 has an expanded stretch with 17 consecutive glutamines. These polyQ tracts have emerged several times throughout evolution, including in the parasitic roundworm species, *Toxocara canis* (GenBank: KHN77343.1). Perhaps the varying lengths of the 14-3-3 polyQ tracts contribute to their individual abilities to form heterotypic interactions with prion-like domains, as has been observed with other polyQ-containing proteins (Gerbich and Gladfelter, 2021; Ripaud et al., 2014). Interestingly, glutamine and asparagine are highly enriched in prion domains, including that of Rim4 (Berchowitz et al., 2015; King et al., 2012). This raises the possibility that Bmh proteins in *S. cerevisiae* have co-evolved with Rim4 to regulate its disassembly.

Do 14–3–3 proteins play a general role in aggregate homeostasis?

Our data demonstrate that 14-3-3 proteins play an important role in clearance of amyloid-like assemblies of Rim4. 14-3-3 proteins interact with hundreds of different binding partners, suggesting that they may play a larger role in protein folding, generally. In support of a general role for 14-3-3 proteins, we found that *bmh*-mutant cells exhibit significantly greater protein aggregate burden as assessed by Hsp104 foci analysis. This snapshot measurement could reflect either increased formation of Hsp104-associated protein aggregates and/or decreased clearance. Our results suggest that the mechanisms that meiotic cells use to coordinate clearance of amyloid-like Rim4 with meiotic progression are, in some way, also important during mitosis for general protein homeostasis. It will be interesting to determine whether 14-3-3 proteins play a similar role in aggregate-associated human diseases.

Limitations of the study

Our data support a role for Bmh1 and Bmh2 in facilitating Rim4 phosphorylation by its kinase, Ime2. We propose that Bmh1 and Bmh2 link Rim4 to Ime2. However, we cannot rule out the possibility that Bmh1 and Bmh2 play indirect roles in Rim4 phosphorylation, potentially by stimulating Ime2 autophosphorylation. Ideally, we would isolate a complex of amyloid-like Rim4, Ime2, and Bmh1/2 and show that the interaction between Ime2 and Rim4 is (partially) dependent on Bmh1/2. This result is challenging for several reasons, one of which being that the interaction between kinases and substrates are often transient and difficult to capture. Further work is necessary to test our models. Secondly, quantitation of immunoblot is a challenge for many reasons. We re-use primary antibodies many times, we experience batch-to-batch variation in our secondary antibodies and our chemiluminescent substrates. We do not run a dilution standard for every experiment. We take several exposures to ensure that our electrochemiluminescent (ECL) signal is linear and not saturated. Our immunoblots are internally, rather than externally, controlled, and we appreciate that this can be an issue for quantitation. In this study, we sometimes show quantification data for immunoblot in which we plot immunoblot signal corrected for loading. We consider these data as semi-quantitative and we provide orthogonal support for conclusions that rely on immunoblot data. Finally, we conclude that Bmh1 and Bmh2 are important for Ime2 association with SDS-resistant assemblies. Although it is likely that Ime2 migrates with SDS-resistant assemblies due to an association with Rim4, additional studies are necessary to demonstrate that this migration pattern depends on Rim4 assembly.

STAR METHODS

RESOURCE AVAILABILITY

Lead Contact—Further information and requests for resources and reagents should be directed to and will be fulfilled by the Lead Contact, Luke Berchowitz (leb2210@cumc.columbia.edu).

Materials availability—All unique/stable reagents generated in this study are available from the lead contact without restriction.

Data and code availability

- Raw mass spectrometry data have been deposited at the MassIVE repository (https://massive.ucsd.edu) and are publicly available as of the date of publication. Accession numbers are listed in the key resources table.
- This paper does not report original code.
- Any additional information required to reanalyze the data reported in this work paper is available from the Lead Contact upon request.

EXPERIMENTAL MODEL AND SUBJECT DETAILS

Yeast strains and constructs—Laboratory strains are described in Table S1. All experiments performed in this study were performed using *S. cerevisiae* strains derived from the SK1 background. *RIM4-3V5*, *IME2st*, *IME2-3V5*, and *IME2st-3V5* is described in (Berchowitz et al., 2013; Carlile and Amon, 2008); *pGAL-NDT80* and *GAL4.ER* are described in (Benjamin et al., 2003); *CLB3-3HA* is described in (Carlile and Amon, 2008); and *rim4*Δ*271C-3V5* is described in (Berchowitz et al., 2015). *RIM4-47A*, *RIm4-27A*, *RIm4-21A*, and *Rim4-10A* are described in (Carpenter et al., 2018). Strains were constructed by crossing and/or using the PCR-based method described in (Longtine et al., 1998) using the SK1 genome reference and annotation from (Yue et al., 2017). PCR and fusion PCR involved templates pFA6a-kanMX6 and pFA6a-His3MX6 (Longtine et al., 1998). *pBMH2-bmh2*Δ*:BMH1* and *pBMH1-bmh1*Δ*:BMH2* strains were constructed by PCR-based mutagenesis. All strains used in this study were verified by sequencing.

METHOD DETAILS

Yeast media details and culture conditions—All yeast strains were grown at 30°C. To generate meiotic cultures, strains were inoculated in YEPD (1% yeast extract, 2% peptone, 2% dextrose) and grown overnight with shaking at 30°C. The following morning, the cells were diluted in BYTA (1% yeast extract, 2% tryptone, 1% potassium acetate, 50 mM potassium phthalate) to an OD_{600} of 0.3 and grown overnight with shaking. The following morning, cells were washed once with water and resuspended in sporulation (SPO) medium (0.3% potassium acetate [pH 7.0], 0.02% raffinose) at OD_{600} = 1.8 and grown with shaking. *pGAL-NDT80*, *GAL4.ER* (*NDT80-IN*) strains were released from G2 arrest by the addition of 1 μM β-estradiol at 6 h.

Meiotic progression analysis and immunofluorescence—Cells were fixed in 3.7% formaldehyde. For the analysis of nuclear divisions and spindle visualization, indirect immunofluorescence was performed as in (Carpenter et al., 2018) with minor modifications. To visualize spindles, we used rat anti-tubulin antibody (BioRad) at a dilution of 1:200, and anti-rat-fluorescein isothiocyanate antibody (Invitrogen) at a dilution of 1:200. Immunofluorescence samples were mounted in ProlongGold (Invitrogen) that included DAPI. Acquisition of images was conducted using a DeltaVision microscope at 100x magnification (GE Healthcare). Spindle morphologies (n = 100 cells per time point) were classified as in (Lee and Amon, 2001). Briefly, metaphase I cells were defined as cells with a single DAPI mass spanned by a short, thick, bipolar, meiotic spindle. Anaphase I cells were defined as cells with two distinct (though not always separated) DAPI masses, and a

single long spindle that spans both DAPI masses. Metaphase II cells were defined as cells with two separate DAPI masses with each spanned by a bipolar, short, thick, meiotic spindle. Anaphase II cells were defined as cells with four distinct (though not always separated) DAPI masses with two long spindles. To detect Rim4, we used a 1:200 dilution of a mouse α-V5 antibody (Invitrogen). The mean intensity of the Rim4 signal was quantified in a 15-pixel diameter circle region of interest (nucleus and vacuole excluded) using ImageJ software.

Denaturing protein sample preparation for immunoblot and immunoprecipitation—Samples were prepared by resuspending the pellet of 4 mL SPO culture in 5% TCA, incubating overnight at 4°C, washing with acetone, and breaking cells using 50 μL acid-washed glass beads (Sigma), 100 μL Lysis Buffer (10 mM Tris-HCl, 1 mM EDTA [pH 8], 2.75 mM DTT, Halt protease inhibitors [ThermoFisher Scientific]), and a 45-s process in a FastPrep-24 (MP Biomedicals) at maximum speed. We added 50 μL Loading Buffer (9% SDS, 0.75 mM Bromophenol blue, 187.5 mM Tris-HCl [pH 6.8], 30% glycerol, and 810 mM β-mercaptoethanol); samples were heated at 100°C for 5 min and centrifuged 5 min at 20,000 g.

Rim4 immunopurification and quantitative mass spectrometry—For native Rim4 IP, 25 mL meiotic culture were pelleted, washed once with Tris (pH 7.5), transferred into a 2-mL tube, and snap frozen in liquid nitrogen for later processing. Cells were broken with Zirconia/Silica beads in 200 mL NP-40 Lysis Buffer (50 mM Tris [pH 7.5], 150 mM NaCl, 1% NP-40, 10% glycerol) containing 1 mM DTT and Halt protease inhibitors (ThermoFisher Scientific). After breaking, extracts were cleared twice by centrifugation at maximum speed at 4°C in a benchtop centrifuge. IPs were performed in extract diluted to 1 mL in NP-40 buffer. Rim4-3V5 was IPed at 4°C 2 h using 20 μL of anti-V5-agarose slurry (Sigma). After incubation, beads were washed four times with NP-40 buffer, twice in Buffer 2 (50 mM Tris [pH 7.5], 150 mM NaCl, 10 mM MgCl2, 0.05% NP-40, and 5% glycerol), and twice in Buffer 3 (50 mM Tris [pH 7.5], 150 mM NaCl, 10 mM MgCl2, and 5% glycerol). After the last wash, the wash buffer was aspirated completely, and the beads were resuspended in 80 μL trypsin buffer (2 M Urea, 50 mM Tris [pH 7.5], 5 μg/mL trypsin) to digest the bound proteins at 37°C for 1 h with agitation. The beads were centrifuged at 100 rcf for 30 s, and the partially digested proteins (the supernatant) were collected. The beads were then washed twice with 60 μL Urea buffer (2 M urea, 50 mM Tris [pH 7.5]). The supernatant of both washes was collected and combined with the partially digested proteins (final volume is 200 μL). After brief centrifugation, the combined partially digested proteins were cleared from residual beads and frozen in liquid nitrogen.

100 μL of the partially digested proteins were thawed and disulfide bonds were reduced with 5 mM dithiothreitol (DTT) and cysteines were subsequently alkylated with 10 mM iodoacetamide. Samples were further digested by adding 0.5 μg sequencing grade modified trypsin (Promega) at 25°C. After 16 h of digestion, samples were acidified with 1% formic acid (final concentration). Tryptic peptides were desalted on C18 StageTips according to (Rappsilber et al., 2007) and evaporated to dryness in a vacuum concentrator. The desalted peptides were labeled with the TMT11plex mass tag labeling reagent according to the

manufacturer's instructions (ThermoFisher Scientific) with small modifications. Briefly, peptides were dissolved in 30 μL of 50 mM HEPES (pH 8.5) solution and the TMT-11plex reagent was added in 12.3 μL of MeCN. The following TMT labels were used: Rim4 IP: 127N, Rim4-ΔIDR IP: 128N, No tag IP: 131N. After 1 h incubation the reaction was stopped with 2.5 μL 5% Hydroxylamine for 15 min at 25°C. Differentially labeled peptides were mixed for each replicate (see mixing scheme below) and subsequently desalted on C18 StageTips (Rappsilber et al., 2007), evaporated to dryness in a vacuum concentrator and reconstituted in 20 μL 3% acetonitrile and 0.1% formic acid.

Liquid chromatography-tandem mass spectrometry was performed as previously described with minor modifications (Cheng et al., 2018; Keshishian et al., 2015). The samples were analyzed on an Eksigent nanoLC-415 HPLC system (Sciex) coupled via a 25-cm C18 column (inner diameter 100 μm packed in house with 2.4 μm ReproSil-Pur C18-AQ medium; Dr. Maisch GmbH) to a benchtop Orbitrap Q Exactive HF mass spectrometer (ThermoFisher Scientific). Peptides were separated at a flow rate of 250 nL/min with a linear 106 min gradient from 2% to 25% solvent B (100% acetonitrile, 0.1% formic acid), followed by a linear 5 min gradient from 25 to 85% solvent B. Each sample was run for 140 min, including sample loading and column equilibration times. Data were acquired in a data-dependent mode using Xcalibur 2.8 software. MS1 Spectra were measured with a resolution of 60,000, an automatic gain control (AGC) target of 3e6 and a mass range from 375 to 2000 m/z. Up to 15 MS2 spectra per duty cycle were triggered at a resolution of 60,000, an AGC target of 2e5, an isolation window of 1.6 m/z, and a normalized collision energy of 36.

All raw data were analyzed with MaxQuant software version 1.6.0.16 (Cox and Mann, 2008) using a UniProt yeast database (release 2014_09, strain ATCC 204508/S288c), and tandem mass spectrometry searches were performed with the following parameters: TMT-11plex labeling on the MS2 level, oxidation of methionine and protein N-terminal acetylation as variable modifications; carbamidomethylation as fixed modification; Trypsin/P as the digestion enzyme; precursor ion mass tolerances of 20 ppm for the first search (used for nonlinear mass re-calibration) and 4.5 ppm for the main search, and a fragment ion mass tolerance of 20 ppm. For identification, we applied a maximum false discovery rate of 1% separately on protein and peptide level. We required one or more unique/razor peptides for protein identification.

Finally, the TMT MS2 intensities were normalized such that at each condition these intensity values added up to exactly 1,000,000; therefore, each protein group value can be regarded as a normalized microshare (we did this separately for each TMT channel for all proteins that made our filter cutoff in all the TMT channels).

Co-IP—2 mL of SPO culture was harvested, centrifuged, and flash frozen in liquid nitrogen. Samples were fully thawed and resuspended in 200 μL NP-40 lysis buffer (50 mM Tris-HCl pH 7.5, 150 mM NaCl, 1% NP-40, 10% glycerol) and protease inhibitors (1: 1,000 DTT, 1: 100 Halt protease inhibitors [ThermoFisher Scientific), 1 mM PMSF) with 0.5-mm zirconia/silica beads (BioSpec Products). Cells were lysed using a 45-s process in a FastPrep-24 (MP Biomedicals) at maximum speed. The lysates were clarified twice by

centrifugation at maximum speed for 10 min at 4°C. Total protein input samples are taken with 10 μL of the lysate and 5 μL 3× loading buffer (9% SDS, 0.75 mM Bromophenol blue, 187.5 mM Tris-HCl [pH 6.8], 30% glycerol, and 810 mM β-mercaptoethanol) and boiling 5 min. The remaining lysate was incubated with 15 μL α-FLAG M2 affinity gel (Sigma) per sample, rotating for 1 h at 4°C. Samples were centrifuged at 2,000 rpm for 30 s. Unbound protein samples were collected with 10 μL lysate and 5 μL 3× loading buffer and boiled for 5 min. The remaining lysate was centrifuged and washed four times with 1 mL NP-40 buffer. The α-FLAG M2 affinity gel beads (Sigma) were incubated in 20 μL 3× loading buffer diluted to 1× in lysis buffer (10 mM Tris-HCl, 1 mM EDTA [pH 8], 2.75 mM DTT, Halt protease inhibitors [ThermoFisher Scientific]), boiled for 5 min and centrifuged 5 min at maximum speed. Samples are then subjected to the immunoblot protocol listed below, and Mouse TrueBlot ULTRA Anti-Mouse Ig horseradish peroxidase (HRP) (Rockland) is used at 1:5,000 for the secondary antibody.

Immunoblot analysis—Polyacrylamide gels were run on a midi gel system (BioRad) with SDS Running Buffer (190 mM glycine, 25 mM Trizma base, 3.5 mM, 1% SDS), using 10% gels loaded with 4 μL sample per well. They were transferred using a semi-dry transfer apparatus (BioRad) to a nitrocellulose membrane. α-HA.11 (BioLegend) was used at 1:1,000, α-Pgk1 (Novex) was used at 1:20,000, α-v5 (Invitrogen) was used at 1:2,000, α-FLAG (Sigma) was used at 1:2,000, α-Bmh1/2 (Gelperin et al., 1995) was used at 1:1,000. An α-mouse HRP-conjugated secondary antibody (GE Healthcare) was used at 1:10,000, 1:20,000, and 1:40,000 for the respective primaries. Signal was visualized using ECL prime chemiluminescence substrate (GE Healthcare) and acquisition of images was conducted using an Amersham Imager 600 (GE Healthcare). At least three exposures were taken for each experiment to ensure that our signal did not saturate and that we were in the linear range of the instrument. To quantify total 14-3-3 protein, we created serial dilutions (1, ½, ¼, 1/8, 1/16, 1/32) of control, 2xBmh1 and 2xBmh2 protein samples to determine the linear range. This assay shows that undiluted samples were saturated, and samples diluted 1:4 were in the linear range.

Northern blot analysis—Samples were harvested as 2 mL of SPO culture, centrifuged, and flash frozen in liquid nitrogen. Pellets were resuspended in 400 μL TES Buffer (10 mM Tris-HCl [pH 7.5], 10 mM EDTA, and 0.5% SDS), 400 μL acid phenol:chloroform 5:1 (Ambion), and 50 μL 0.5 mm zirconia/silica beads (BioSpec). Cells were lysed by shaking at 1,400 rpm for 30 min at 65°C in a Thermomixer (Eppendorf) followed by centrifugation for 5 min at 13,000 g, extraction to 1 mL 100% ethanol and 40 μL sodium acetate (pH 5.5), and precipitation at −20°C overnight.

Samples were centrifuged at 13,000 g for 20 min, washed with 1 mL 80% ethanol, centrifuged at 13,000 g for 5 min, and dried. RNA pellets were resuspended in 25 μL DEPC water at 37°C with shaking at 1000 rpm for 15 min and concentrations were determined using a NanoDrop (ThermoFisher Scientific). We added 22 μL denaturing mix (15 μL formamide, 5.5 μL formaldehyde, and 1.5 μL 10× MOPS) to 8 μg total RNA in 8 μL and heated at 55°C for 15 min 20 μL of sample (approximately 5 μg) was resolved on a denaturing agarose gel (1.9% agarose, 3.7% formaldehyde, 1× MOPS buffer) for 2.5 h at

80 V. The gel was blotted to a Hybond membrane (GE Healthcare) by capillary transfer in 10× SSC (1.5 M NaCl, 0.15 M trisodium citrate dihydrate, [pH 7]). The membrane was incubated in a hybridization buffer (0.25 M Na-phosphate [pH 7.2], 0.25 M NaCl, 1 mM EDTA, 7% SDS, and 5% dextran sulfate) at 65°C probed with ^{32}P-labeled *CLB3* DNA probes prepared via Amersham Megaprime DNA labeling kit (GE Healthcare) and Illustra ProbeQuant columns (GE Healthcare), transferred to a phosphor screen, and imaged on a Typhoon imager (GE Healthcare).

Blot quantification—Immunoblot and Northern blot experiments were quantified using FIJI (ImageJ) software. Signal intensity was normalized to a loading control (Pgk1 for immunoblots and *rRNA* for Northerns).

SDD-AGE—SDD-AGE was adapted from previous protocols as described in (Halfmann and Lindquist, 2008). The 2 mL samples of sporulating culture were harvested by centrifugation and snap frozen in liquid nitrogen. Cell pellets were resuspended in 200 µL lysis buffer (100 mM Tris/HCl [pH 8.0], 20 mM $NaCl_2$, 2 mM $MgCl_2$, 50 mM β-mercaptoethanol, 1% Triton X-, 2× Halt protease inhibitors [Thermo-Fisher Scientific]) and broken using a FastPrep-24 and 0.5 mm zirconia/silica beads (BioSpec). The lysates were clarified twice by centrifugation at 2,500 rcf for 5 min at 4°C. 4× sample loading buffer (final concentration 0.5× TAE, 5% glycerol, 2% SDS, bromophenol blue) was added to lysates, which were incubated for 10 min at room temperature. After incubation, 20 µL of each sample was separated on a 1.7% agarose 0.5× TAE +0.1% SDS gel for 16 h at 25 V at 4°C using 0.5× TAE supplemented with 0.1% SDS as the running buffer. A peristaltic pump was used to recirculate the running buffer at 3 mL/min. The gel was blotted to nitrocellulose (GE Healthcare) by capillary transfer in 1× TBS and processed by the immunoblot procedure outlined above. α-v5 (Invitrogen) or α-FLAG (Sigma) was used at 1:2,000 with α-mouse HRP-conjugated secondary antibody (GE Healthcare) at 1:5,000.

Immunopurification of Bmh1, Bmh2, and Ime^{2st} from yeast—For purification of Bmh1 and Bmh2, samples were harvested as 1 L of YPD culture grown overnight at 30°C while shaking. For purification of both Bmh1 and Bmh2, samples were harvested from a strain containing *BMH1-3FLAG* (B1421). Anti-FLAG results in purification of both Bmh proteins owing to the heterodimeric interaction between Bmh1 and Bmh2. For purification of Bmh1-3FLAG without Bmh2, samples were harvested from *BMH1-3FLAG*, *bmh2*Δ cells (B2535). Similarly, for the purification of Bmh2-3FLAG without Bmh1, samples were harvested from *bmh1*Δ, *BMH2-3FLAG* cells (B2537). Ime2st was purified as in (Phizicky et al., 2018) with minor modifications. Briefly, 1 L cells containing *pGAL-IME2-3FLAG* (B114) were induced to express *IME2* by the addition of 2% galactose to the growth media.

Samples were centrifuged, and flash frozen in liquid nitrogen. Samples were fully thawed and resuspended in 5 mL NP-40 lysis buffer (50 mM Tris-HCl pH 7.5, 150 mM NaCl, 1% NP-40, 10% glycerol, 1 mM DTT) and Halt protease inhibitors (ThermoFisher Scientific), 1 mM PMSF). Cells were mechanically lysed with 0.5 mm zirconia/silica beads (BioSpec Products), in a FastPrep-24 (MP Biomedicals) at maximum speed (2 × 45 s). The lysates were clarified twice by centrifugation at maximum speed for 10 min at 4°C. Lysate was incubated with 1.5 mL α-FLAG M2 affinity gel (Sigma) overnight at 4°C. The affinity gel

was collected by centrifugation at 2,000 rpm for 2 min and washed (×4) with 5 mL NP-40 buffer (50 mM Tris-HCl pH 7.5, 150 mM NaCl, 1% NP-40, 10% glycerol) and placed into a disposable 10 mL polypropylene column (ThermoFisher Scientific). After draining the final wash, the gel was incubated 30 min with Elution Buffer (1 mL NP-40 buffer, 0.15 mg/mL FLAG peptide [APExBIO]). The elution was concentrated by ultrafiltration and run over a Superdex 200 column (GE Healthcare). The fractions containing the proteins of interest were pooled.

Expression and purification of assembled Rim4—Purification of the assembled Rim4 was done as in (Berchowitz et al., 2015) with modifications. Four liters of LOBSTR cells (Andersen et al., 2013) containing a *RIM4-14HIS* plasmid were grown in LB (with 100 μg/mL of ampicillin and 35 μ/mL of chloramphenicol) to an OD_{600} of 0.7 at 37°C, shifted to 18°C for 30 min, and induced with 200 μM IPTG for 18 h. The cells were collected by centrifugation and resuspended in 400 mL of cold lysis buffer (50 mM Tris/HCl pH 8.0, 500 mM NaCl, 40 mM imidazole, and 5 mM β-mercaptoethanol). The cells were lysed by sonication. DNase and PMSF (1 mM final concentration) were added to the cells post-lysis. Cell debris was removed by centrifugation and the supernatant was incubated with 1 mL of equilibrated Ni-Sepharose 6 Fast Flow resin (GE Life Sciences) and gently mixed in batch for 1 h at 4°C. The Ni-resin was collected by centrifugation and placed into a disposable 10 mL polypropylene column (Thermo Fisher Scientific) and washed with 10 column volumes of wash buffer (10 mM Tris/HCl pH 8.0, 150 mM NaCl, 40 mM imidazole, and 5 mM β-mercaptoethanol). Rim4 was eluted with 25 mL of elution buffer (10 mM Tris/HCl pH 8.0, 150 mM NaCl, 300 mM imidazole, and 5 mM β-mercaptoethanol). The elution (25 mL) was concentrated by ultrafiltration and run over a Superose 6 Increase (GE Healthcare) size exclusion column. Finally, the void fractions corresponding to assembled Rim4 were pooled and concentrated by ultrafiltration.

***In vitro* kinase assay—**Rim4 (2 μM) and $Ime2^{st}$ (2 μM) were incubated in kinase buffer (25 mM Tris-HCl [pH 7.5], 5 mM beta-glycerophosphate, 1 mM DTT, 0.1 mM Na_3VO_4, 10 mM $MgCl_2$, 10 mM ATP [non-radioactive]) alone or with Bmh1 (6.67 μM), Bmh2 (6.67 μM), or Bmh1 and Bmh2 protein purified from yeast. BSA was added as a control for molecular crowding (equivalent w/v) in samples without Bmh1, Bmh2, or both. The reaction was initiated by adding 1 μL of [γ-^{32}P] ATP (3,000 Ci/mmol) to each sample. The 5-μL samples were withdrawn after the indicated amount of time. To stop the reaction, 2.5 μL 3× SDS loading buffer (9% SDS, 0.75 mM Bromophenol blue, 187.5 mM Tris-HCl [pH 6.8], 30% glycerol, and 810 mM β-mercaptoethanol) was added and samples were boiled for 5 min. Samples were separated on a 10% SDS-PAGE gel and transferred to a nitrocellulose membrane using a semi-dry transfer (BioRad). The membrane was dried, mounted on a phosphor screen, and imaged on a Typhoon imager (GE Healthcare). Loading of Bmh1, Bmh2, and $Ime2^{st}$ was analyzed by anti-FLAG immunoblot.

QUANTIFICATION AND STATISTICAL ANALYSIS

Immunoblot and Northern blot were quantified using FIJI software (Schindelin et al., 2012). Signal intensity was normalized to a loading control (Pgk1 for immunoblots, 25S *rRNA* for Northern blots). Values were multiplied by an arbitrary scaling factor, which was held

constant within each figure panel for each technique. Statistical significance was determined by the Student's t test, Mann-Whitney test, or Z-test statistic as indicated. We used Prism 9 software to determine whether our data met the assumptions of each statistical approach. In cases of non-normal data distributions, we analyzed statistical significance using a non-parametric Mann-Whitney U test. The number of biological replicates and exact values of n are indicated in figure legends where applicable.

Supplementary Material

Refer to Web version on PubMed Central for supplementary material.

ACKNOWLEDGMENTS

We thank Sandra Lemmon for providing the anti-Bmh1/2 antibody. We also thank David Phizicky and Stephen Bell for Ime2 expression strains and Heather Feaga for Ime2 purification. We thank Gizem Dursuk and Nadja Zhakula-Kostadinova for help with experimental procedures. We thank Raphaelle Laureau for bioinformatics help and figure design. Last, we thank Raphaelle Laureau, Diana Ottoz, and Rodney Rothstein for valuable discussion and for editing the manuscript. This research is supported by The Schaefer Research Scholars Program, The Hirschl Family Trust, and NIH grants R35 GM124633 to L.E.B and R35 GM128802 to M.J.

REFERENCES

Agarwal-Mawal A, Qureshi HY, Cafferty PW, Yuan Z, Han D, Lin R, and Paudel HK (2003). 14-3-3 Connects glycogen synthase kinase-3β to tau within a brain microtubule-associated tau phosphorylation complex. J. Biol. Chem. 278, 12722–12728. [PubMed: 12551948]

Alberti S, Halfmann R, King O, Kapila A, and Lindquist S (2009). A systematic survey identifies prions and illuminates sequence features of prionogenic proteins. Cell 137, 146–158. [PubMed: 19345193]

Andersen KR, Leksa NC, and Schwartz TU (2013). Optimized *E. coli* expression strain LOBSTR eliminates common contaminants from His-tag purification. Proteins Struct. Funct. Bioinforma. 81, 1857–1861.

Benjamin KR, Zhang C, Shokat KM, and Herskowitz I (2003). Control of landmark events in meiosis by the CDK Cdc28 and the meiosis-specific kinase Ime2. Genes Dev. 17, 1524–1539. [PubMed: 12783856]

Berchowitz LE, Gajadhar AS, van Werven FJ, De Rosa AA, Samoylova ML, Brar GA, Xu Y, Xiao C, Futcher B, Weissman JS, et al. (2013). A developmentally regulated translational control pathway establishes the meiotic chromosome segregation pattern. Genes Dev. 27, 2147–2163. [PubMed: 24115771]

Berchowitz LE, Kabachinski G, Walker MR, Carlile TM, Gilbert WV, Schwartz TU, and Amon A (2015). Regulated formation of an amyloid-like translational repressor governs gametogenesis. Cell 163, 406–418. [PubMed: 26411291]

Berg D, Holzmann C, and Riess O (2003). 14-3-3 proteins in the nervous system. Nat. Rev. Neurosci. 4, 752–762. [PubMed: 12951567]

Biernat J, Gustke N, Drewes G, Mandelkow E, and Mandelkow E (1993). Phosphorylation of Ser262 strongly reduces binding of tau to microtubules: distinction between PHF-like immunoreactivity and microtubule binding. Neuron 11, 153–163. [PubMed: 8393323]

Carlile TM, and Amon A (2008). Meiosis I is established through division-specific translational control of a cyclin. Cell 133, 280–291. [PubMed: 18423199]

Carpenter K, Bell RB, Yunus J, Amon A, and Berchowitz LE (2018). Phosphorylation-mediated clearance of amyloid-like assemblies in meiosis. Dev. Cell 45, 392–405.e6. [PubMed: 29738715]

Chan TA, Hermeking H, Lengauer C, Kinzler KW, and Vogelstein B (1999). 14-3-3σ is required to prevent mitotic catastrophe after DNA damage. Nature 401, 616–620. [PubMed: 10524633]

Chaudhri M, Scarabel M, and Aitken A (2003). Mammalian and yeast 14-3-3 isoforms form distinct patterns of dimers *in vivo*. Biochem. Biophys. Res. Commun. 300, 679–685. [PubMed: 12507503]

Chen HK, Fernandez-Funez P, Acevedo SF, Lam YC, Kaytor MD, Fernandez MH, Aitken A, Skoulakis EMC, Orr HT, Botas J, et al. (2003). Interaction of Akt-phosphorylated ataxin-1 with 14-3-3 mediates neurodegeneration in spinocerebellar ataxia type 1. Cell 113, 457–468. [PubMed: 12757707]

Cheng Z, Otto GM, Powers EN, Keskin A, Mertins P, Carr SA, Jovanovic M, and Brar GA (2018). Pervasive, coordinated protein-level changes driven by transcript isoform switching during meiosis. Cell 172, 910–923.e16. [PubMed: 29474919]

Chernoff YO, Lindquist SL, Ono BI, Inge-Vechtomov SG, and Liebman SW (1995). Role of the chaperone protein Hsp104 in propagation of the yeast prion-like factor [psi+]. Science 268, 880–884. [PubMed: 7754373]

Cox J, and Mann M (2008). MaxQuant enables high peptide identification rates, individualized p.p.b.-range mass accuracies and proteome-wide protein quantification. Nat. Biotechnol. 26, 1367–1372. [PubMed: 19029910]

Deng C, and Saunders W (2001). RIM4 encodes a meiotic activator required for early events of meiosis in *Saccharomyces cerevisiae*. Mol. Genet. Genomics. 266, 497–504. [PubMed: 11713679]

Foote M, and Zhou Y (2012). 14-3-3 proteins in neurological disorders. Int. J. Biochem. Mol. Biol. 3, 152–164. [PubMed: 22773956]

Ford JC, Al-Khodairy F, Fotou E, Sheldrick KS, Griffiths DJF, and Carr AM (1994). 14-3-3 Protein homologs required for the DNA damage checkpoint in fission yeast. Science 265, 533–535. [PubMed: 8036497]

Fujiwara H, Hasegawa M, Dohmae N, Kawashima A, Masliah E, Goldberg MS, Shen J, Takio K, and Iwatsubo T (2002). α-synuclein is phosphorylated in synucleinopathy lesions. Nat. Cell Biol. 4, 160–164. [PubMed: 11813001]

Garcia-Mata R, Gao YS, and Sztul E (2002). Hassles with taking out the garbage: aggravating aggresomes. Traffic 3, 388–396. [PubMed: 12010457]

Gelbart ME, Rechsteiner T, Richmond TJ, and Tsukiyama T (2001). Interactions of Isw2 chromatin remodeling complex with nucleosomal arrays: analyses using recombinant yeast histones and immobilized templates. Molecular and cellular biology 21 (6), 2098–2106. [PubMed: 11238944]

Gelperin D, Weigle J, Nelson K, Roseboom P, Irie K, Matsumoto K, and Lemmon S (1995). 14-3-3 Proteins: potential roles in vesicular transport and Ras signaling in *Saccharomyces cerevisiae*. Proc. Natl. Acad. Sci. U S A 92, 11539–11543. [PubMed: 8524799]

Gerbich TM, and Gladfelter AS (2021). Moving beyond disease to function: physiological roles for polyglutamine-rich sequences in cell decisions. Curr. Opin. Cell Biol. 69, 120–126. [PubMed: 33610098]

Glover JR, and Lindquist S (1998). Hsp104, Hsp70, and Hsp40: a novel chaperone system that rescues previously aggregated proteins. Cell 94, 73–82. [PubMed: 9674429]

Gong C-X, Singh TJ, Grundke-Iqbal I, and Iqbal K (1993). Phosphoprotein phosphatase activities in alzheimer disease brain. J. Neurochem. 61, 921–927. [PubMed: 8395566]

Halfmann R, and Lindquist S (2008). Screening for amyloid aggregation by semi-denaturing detergent-agarose gel electrophoresis. J. Vis. Exp, 838. [PubMed: 19066511]

Hashiguchi M, Sobue K, and Paudel HK (2000). 14-3-3ζ is an effector of tau protein phosphorylation. J. Biol. Chem. 275, 25247–25254. [PubMed: 10840038]

Hernández F, Cuadros R, and Avila J (2004). Zeta 14-3-3 protein favours the formation of human tau fibrillar polymers. Neurosci. Lett. 357, 143–146. [PubMed: 15036595]

Van Heusden GPH, Griffiths DJF, Ford JC, Chin-A-Woeng TFC, Schrader PAT, Carr AM, and Steensma HY (1995). The 14-3-3 proteins encoded by the BMH1 and BMH2 genes are essential in the yeast *Saccharomyces cerevisiae* and can be replaced by a plant homologue. Eur. J. Biochem. 229, 45–53. [PubMed: 7744048]

Jafar-Nejad P, Ward CS, Richman R, Orr HT, and Zoghbi HY (2011). Regional rescue of spinocerebellar ataxia type 1 phenotypes by 14-3-3e haploinsufficiency in mice underscores complex pathogenicity in neurodegeneration. Proc. Natl. Acad. Sci. U S A 108, 2142–2147. [PubMed: 21245341]

Jeganathan S, Hascher A, Chinnathambi S, Biernat J, Mandelkow EM, and Mandelkow E (2008). Proline-directed pseudo-phosphorylation at AT8 and PHF1 epitopes induces a compaction of the paperclip folding of tau and generates a pathological (MC-1) conformation. J. Biol. Chem. 283, 32066–32076. [PubMed: 18725412]

Jicha GA, O'Donnell A, Weaver C, Angeletti R, and Davies P (1999). Hierarchical phosphorylation of recombinant tau by the paired-helical filament-associated protein kinase is dependent on cyclic AMP-dependent protein kinase. J. Neurochem. 72, 214–224. [PubMed: 9886072]

Kane SM, and Roth R (1974). Carbohydrate metabolism during ascospore development in yeast. Journal of bacteriology 118 (1), 8–14. [PubMed: 4595206]

Kaplan A, Morquette B, Kroner A, Leong SY, Madwar C, Sanz R, Banerjee SL, Antel J, Bisson N, David S, et al. (2017). Small-molecule stabilization of 14-3-3 protein-protein interactions stimulates axon regeneration. Neuron 93, 1082–1093.e5. [PubMed: 28279353]

Keshishian H, Burgess MW, Gillette MA, Mertins P, Clauser KR, Mani DR, Kuhn EW, Farrell LA, Gerszten RE, and Carr SA (2015). Multiplexed, quantitative workflow for sensitive biomarker discovery in plasma yields novel candidates for early myocardial injury. Mol. Cell. Proteomics MCP 14, 2375–2393. [PubMed: 25724909]

Khan MR, Li L, Pérez-Sánchez C, Saraf A, Florens L, Slaughter BD, Unruh JR, and Si K (2015). Amyloidogenic oligomerization transforms *Drosophila* Orb2 from a translation repressor to an activator. Cell 163, 1468–1483. [PubMed: 26638074]

King OD, Gitler AD, and Shorter J (2012). The tip of the iceberg: RNA-binding proteins with prion-like domains in neurodegenerative disease. Brain Res. 1462, 61–80. [PubMed: 22445064]

Knowles TPJ, Vendruscolo M, and Dobson CM (2014). The amyloid state and its association with protein misfolding diseases. Nat. Rev. Mol. Cell Biol. 15, 384–396. [PubMed: 24854788]

Kopke E, Tung YC, Shaikh S, Del Alonso CA, Iqbal K, and Grundke-Iqbal I (1993). Microtubule-associated protein tau. Abnormal phosphorylation of a non- paired helical filament pool in Alzheimer disease. J. Biol. Chem. 268, 24374–24384. [PubMed: 8226987]

Kryndushkin DS, Alexandrov IM, Ter-Avanesyan MD, and Kushnirov VV (2003). Yeast [PSI+] prion aggregates are formed by small Sup35 polymers fragmented by Hsp104. J. Biol. Chem. 278, 49636–49643. [PubMed: 14507919]

Layfield R, Fergusson J, Aitken A, Lowe J, Landon M, and Mayer RJ (1996). Neurofibrillary tangles of Alzheimer's disease brains contain 14-3-3 proteins. Neurosci. Lett. 209, 57–60. [PubMed: 8734909]

Lee B, and Amon A (2001). Meiosis: how to create a specialized cell cycle. Curr. Opin. Cell Biol. 13, 770–777. [PubMed: 11698195]

Lee HJ, Shin SY, Choi C, Lee YH, and Lee SJ (2002). Formation and removal of α-synuclein aggregates in cells exposed to mitochondrial inhibitors. J. Biol. Chem. 277, 5411–5417. [PubMed: 11724769]

Leysen S, Burnley RJ, Rodriguez E, Milroy LG, Soini L, Adamski CJ, Nitschke L, Davis R, Obsil T, Brunsveld L, et al. (2021). A structural study of the cytoplasmic chaperone effect of 14-3-3 proteins on ataxin-1. J. Mol. Biol. 433, 167174. [PubMed: 34302818]

Li T, and Paudel HK (2007). 14-3-3ζ Facilitates GSK3β-catalyzed tau phosphorylation in HEK-293 cells by a mechanism that requires phosphorylation of GSK3b on Ser9. Neurosci. Lett. 414, 203–208. [PubMed: 17317006]

Liebman SW, and Chernoff YO (2012). Prions in yeast. Genetics 42, 337–345.

Longtine MS, McKenzie A, Demarini DJ, Shah NG, Wach A, Brachat A, Philippsen P, and Pringle JR (1998). Additional modules for versatile and economical PCR-based gene deletion and modification in *Saccharomyces cerevisiae*. Yeast 14, 953–961. [PubMed: 9717241]

Madeira F, Tinti M, Murugesan G, Berrett E, Stafford M, Toth R, Cole C, MacKintosh C, and Barton GJ (2015). 14-3-3-Pred: improved methods to predict 14-3-3-binding phosphopeptides. Bioinformatics 31, 2276–2283. [PubMed: 25735772]

Maji SK, Perrin MH, Sawaya MR, Jessberger S, Vadodaria K, Rissman RA, Singru PS, Nilsson KPR, Simon R, Schubert D, et al. (2009). Functional amyloids as natural storage of peptide hormones in pituitary secretory granules. Science 325, 328–332. [PubMed: 19541956]

Miller MP, Ünal E, Brar GA, and Amon A (2012). Meiosis I chromosome segregation is established through regulation of microtubule–kinetochore interactions. Elife 1, e00117. [PubMed: 23275833]

Monahan Z, Ryan VH, Janke AM, Burke KA, Rhoads SN, Zerze GH, O'Meally R, Dignon GL, Conicella AE, Zheng W, et al. (2017). Phosphorylation of the FUS low-complexity domain disrupts phase separation, aggregation, and toxicity. EMBO J 36, 2951–2967. [PubMed: 28790177]

Morawska M, and Ulrich HD (2013). An expanded tool kit for the auxin-inducible degron system in budding yeast. Yeast 30, 341–351. [PubMed: 23836714]

Narayanan S, Walter S, and Reif B (2006). Yeast prion-protein, Sup35, fibril formation proceeds by addition and substraction of oligomers. ChemBioChem 7, 757–765. [PubMed: 16570324]

Newby GA, and Lindquist S (2013). Blessings in disguise: biological benefits of prion-like mechanisms. Trends Cell Biol. 23, 251–259. [PubMed: 23485338]

Obsil T, Ghirlando R, Klein DC, Ganguly S, and Dyda F (2001). Crystal structure of the 14-3-3ζ:serotonin N-acetyltransferase complex: a role for scaffolding in enzyme regulation. Cell 105, 257–267. [PubMed: 11336675]

Phizicky DV, Berchowitz LE, and Bell SP (2018). Multiple kinases inhibit origin licensing and helicase activation to ensure reductive cell division during meiosis. Elife 7, e33309. [PubMed: 29388912]

Rappsilber J, Mann M, and Ishihama Y (2007). Protocol for micro-purification, enrichment, pre-fractionation and storage of peptides for proteomics using StageTips. Nat Protoc. 2, 1896–1906. [PubMed: 17703201]

Ripaud L, Chumakova V, Antonin M, Hastie AR, Pinkert S, Körner R, Ruff KM, Pappu RV, Hornburg D, Mann M, et al. (2014). Overexpression of Q-rich prion-like proteins suppresses polyQ cytotoxicity and alters the polyQ interactome. Proc. Natl. Acad. Sci. U S A 111, 18219–18224. [PubMed: 25489109]

Rittinger K, Budman J, Xu J, Volinia S, Cantley LC, Smerdon SJ, Gamblin SJ, and Yaffe MB (1999). Structural analysis of 14-3-3 phosphopeptide complexes identifies a dual role for the nuclear export signal of 14-3-3 in ligand binding. Mol. Cell. 4, 153–166. [PubMed: 10488331]

Ruberg FL, Grogan M, Hanna M, Kelly JW, and Maurer MS (2019). Transthyretin amyloid cardiomyopathy: JACC state-of-the-art review. J. Am. Coll. Cardiol. 73, 2872–2891. [PubMed: 31171094]

Sanchez Y, and Lindquist SL (1990). HSP104 required for induced thermotolerance. Science 248, 1112–1115. [PubMed: 2188365]

Sanchez Y, Taulien J, Borkovich KA, and Lindquist S (1992). Hsp104 is required for tolerance to many forms of stress. EMBO J. 11, 2357–2364. [PubMed: 1600951]

Sawyer EM, Joshi PR, Jorgensen V, Yunus J, Berchowitz LE, and Ünal E (2019). Developmental regulation of an organelle tether coordinates mitochondrial remodeling in meiosis. Journal of Cell Biology 218 (2), 559–579. [PubMed: 30538140]

Schindelin J, Arganda-Carreras I, Frise E, Kaynig V, Longair M, Pietzsch T, Preibisch S, Rueden C, Saalfeld S, and Schmid B (2012). Fiji: an open-source platform for biological-image analysis. Nat. Methods 9, 676–682. [PubMed: 22743772]

Schindler K, and Winter E (2006). Phosphorylation of Ime2 regulates meiotic progression in *Saccharomyces cerevisiae*. J. Biol. Chem. 281, 18307–18316. [PubMed: 16684773]

Shorter J, and Lindquist S (2006). Destruction or potentiation of different prions catalyzed by similar Hsp104 remodeling activities. Mol. Cell 23, 425–438. [PubMed: 16885031]

Sia RA, and Mitchell AP (1995). Stimulation of later functions of the yeast meiotic protein kinase Ime2p by the IDS2 gene product. Mol. Cell. Biol. 15, 5279–5287. [PubMed: 7565676]

Slubowski CJ, Paulissen SM, and Huang LS (2014). The GCKIII kinase Sps1 and the 14-3-3 Isoforms, Bmh1 and Bmh2, cooperate to ensure proper sporulation in *Saccharomyces cerevisiae*. PLoS One 9, e113528. [PubMed: 25409301]

Snaith HA, Samejima I, and Sawin KE (2005). Multistep and multimode cortical anchoring of tea1p at cell tips in fission yeast. The EMBO journal 24 (21), 3690–3699. [PubMed: 16222337]

Sopko R, Raithatha S, and Stuart D (2002). Phosphorylation and maximal activity of *Saccharomyces cerevisiae* meiosis-specific transcription factor Ndt80 is dependent on Ime2. Mol. Cell. Biol. 22, 7024–7040. [PubMed: 12242283]

Soushko M, and Mitchell AP (2000). An RNA-binding protein homologue that promotes sporulation-specific gene expression in *Saccharomyces cerevisiae*. Yeast 16, 631–639. [PubMed: 10806425]

Steinacker P, Aitken A, and Otto M (2011). 14-3-3 proteins in neurodegeneration. Semin. Cell Dev. Biol. 22, 696–704. [PubMed: 21920445]

Tenreiro S, Eckermann K, and Outeiro TF (2014). Protein phosphorylation in neurodegeneration: friend or foe? Front. Mol. Neurosci. 7, 42.

Underwood R, Gannon M, Pathak A, Kapa N, Chandra S, Klop A, and Yacoubian TA (2021). 14-3-3 mitigates alpha-synuclein aggregation and toxicity in the in vivo preformed fibril model. Acta Neuropathol. Commun. 9, 13. [PubMed: 33413679]

Waelter S, Boeddrich A, Lurz R, Scherzinger E, Lueder G, Lehrach H, and Wanker EE (2001). Accumulation of mutant huntingtin fragments in aggresome-like inclusion bodies as a result of insufficient protein degradation. Mol. Biol. Cell. 12, 1393–1407. [PubMed: 11359930]

Wang B, Underwood R, Kamath A, Britain C, McFerrin MB, McLean PJ, Volpicelli-Daley LA, Whitaker RH, Placzek WJ, Becker K, et al. (2018). 14-3-3 proteins reduce cell-to-cell transfer and propagation of pathogenic alpha-synuclein. J. Neurosci. 38, 8211–8232. [PubMed: 30093536]

Wang F, Zhang R, Feng W, Tsuchiya D, Ballew O, Li J, Denic V, and Lacefield S (2020). Autophagy of an amyloid-like translational repressor regulates meiotic exit. Dev. Cell. 52, 141–151.e5. [PubMed: 31991104]

Wang Y, Meriin AB, Zaarur N, Romanova NV, Chernoff YO, Costello CE, and Sherman MY (2009). Abnormal proteins can form aggresome in yeast: aggresome-targeting signals and components of the machinery. FASEB J 23, 451–463. [PubMed: 18854435]

Watanabe A, Hasegawa M, Suzuki M, Takio K, Morishima-Kawashima M, Titani K, Arai T, Kosik KS, and Ihara Y (1993). *In vivo* phosphorylation sites in fetal and adult rat tau. J. Biol. Chem. 268, 25712–25717. [PubMed: 8245007]

Wilker EW, Van Vugt MATM, Artim SA, Huang PH, Petersen CP, Reinhardt HC, Feng Y, Sharp PA, Sonenberg N, White FM, et al. (2007). 14-3-3σ controls mitotic translation to facilitate cytokinesis. Nature 446, 329–332. [PubMed: 17361185]

Xu Z, Graham K, Foote M, Liang F, Rizkallah R, Hurt M, Wang Y, Wu Y, and Zhou Y (2013). 14-3-3 protein targets misfolded chaperone-associated proteins to aggresomes. J. Cell Sci. 126, 4173–4186. [PubMed: 23843611]

Yaffe MB (2002). How do 14-3-3 proteins work? - gatekeeper phosphorylation and the molecular anvil hypothesis. FEBS Lett. 513, 53–57. [PubMed: 11911880]

Yuan Z, Agarwal-Mawal A, and Paudel HK (2004). 14-3-3 Binds to and mediates phosphorylation of microtubule-associated tau protein by Ser9-phosphorylated glycogen synthase kinase 3b in the brain. J. Biol. Chem. 279, 26105–26114. [PubMed: 15073173]

Yue JX, Li J, Aigrain L, Hallin J, Persson K, Oliver K, Bergström A, Coupland P, Warringer J, Lagomarsino MC, et al. (2017). Contrasting evolutionary genome dynamics between domesticated and wild yeasts. Nat. Genet. 49, 913–924. [PubMed: 28416820]

Zoghbi HY, and Orr HT (1995). Spinocerebellar ataxia type 1. Semin. Cell Biol. 5, 24.

Highlights

- Yeast 14-3-3 proteins Bmh1 and Bmh2 bind to Rim4 amyloidlike assemblies in meiosis
- Bmh1 and Bmh2 act non-redundantly in phosphorylation-mediated clearance of Rim4
- 14-3-3 proteins facilitate Rim4 phosphorylation by Ime2
- 14-3-3 proteins contribute to global protein aggregate homeostasis

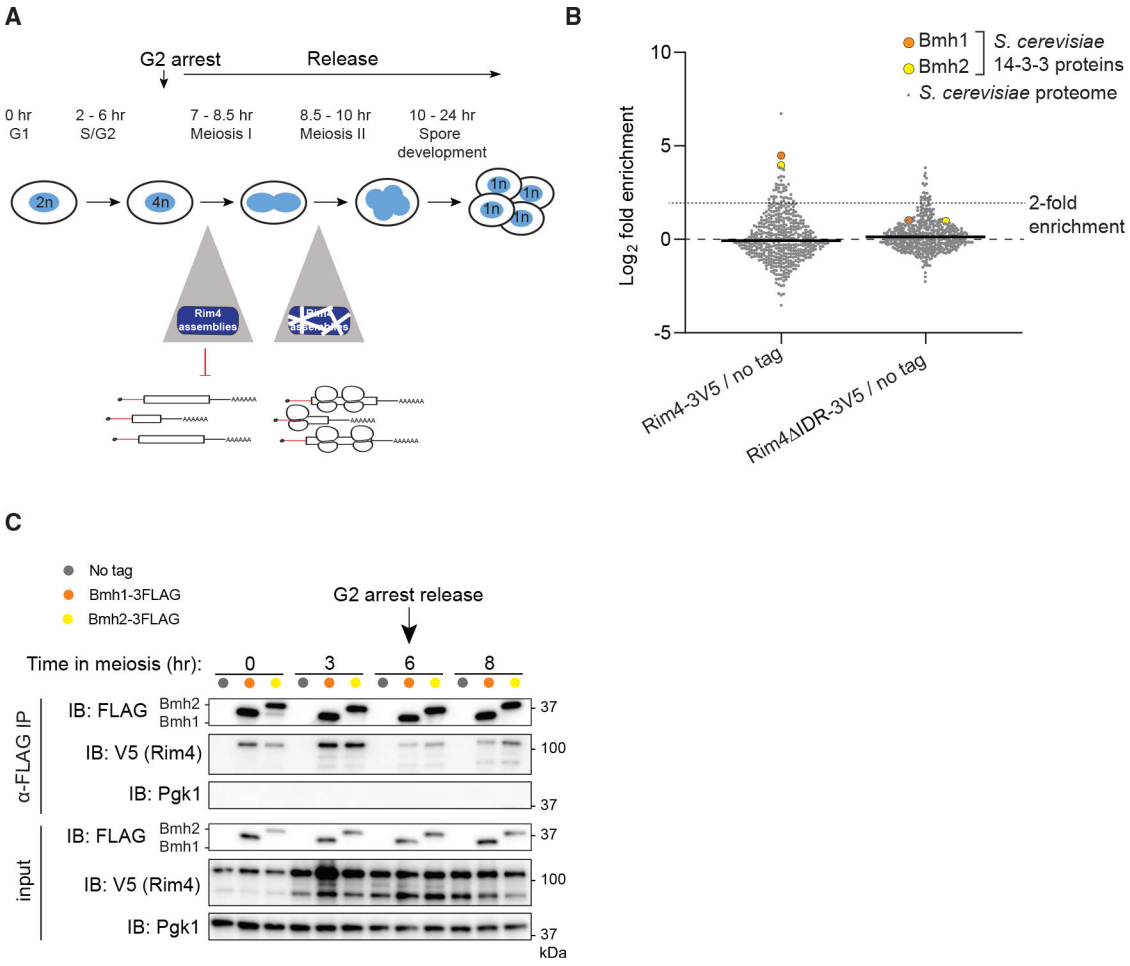

Figure 1. Assembled Rim4 interacts with the yeast 14-3-3 proteins Bmh1 and Bmh2

(A) Schematic showing meiosis progression and Rim4 activity status in *NDT80-IN* (*NDT80*-inducible) strains.

(B) Strains harboring *NDT80-IN* and either *RIM4–3V5* (B48), *rim4ΔIDR-3V5* (A35408), or a no tag control (A15055) were induced to sporulate at 30°C. At 6 h, when cells had arrested in G2 owing to the lack of Ndt80, cells were collected. Lysates were prepared and Rim4 IP was conducted under non-denaturing conditions using anti-V5 agarose beads. Precipitated proteins were TMT-labeled and analyzed by mass spectrometry. Shown are the Log_2 ratios of enrichment over a no-tag control for each identified protein (min 2 unique peptides).

(C) Strains harboring *NDT80-IN*, *RIM4–3V5*, and untagged *BMH* (B48, gray), *BMH1-FLAG* (B2169, orange) or *BMH2-FLAG* (B2170, yellow) were induced to sporulate at 30°C. Cells were released from the G2 arrest at 6 h. Bmh1-FLAG or Bmh2-FLAG was IPed from meiotic lysate using anti-FLAG agarose beads at the indicated time points. Shown are Bmh1, Bmh2, Rim4, and Pgk1 (non-interacting/loading control) protein levels by immunoblot in IP and input samples. (Biological replicates >5).

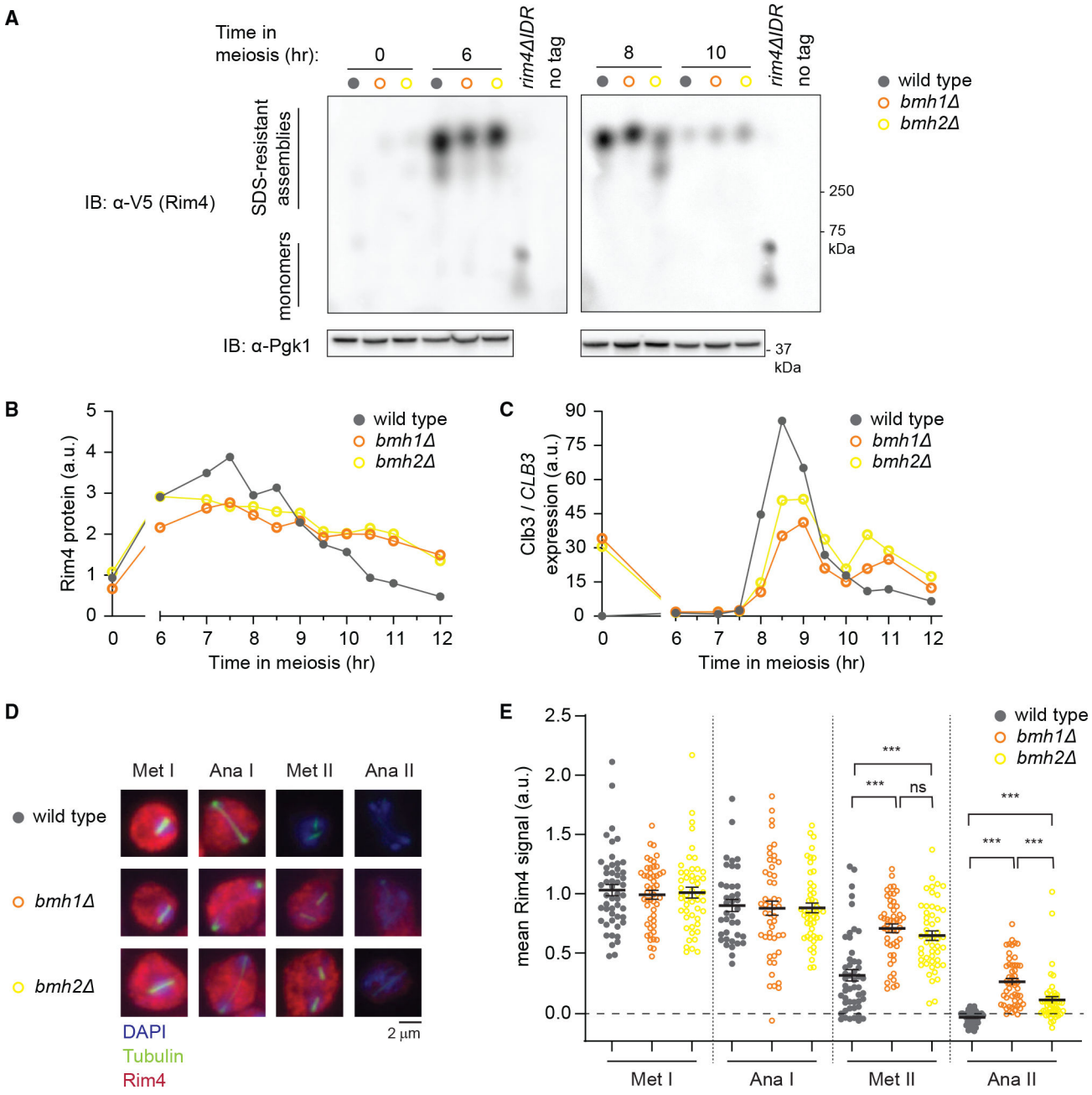

Figure 2. Bmh1 and Bmh2 are critical for timely clearance of Rim4 assemblies

Strains harboring *NDT80-IN*, *RIM4–3V5*, *CLB3–3HA*, and either *bmh1*Δ (B668, orange), *bmh2*Δ (B442, yellow) or wild-type *BMH1/2* (B48, gray) were induced to sporulate at 30°C. Cells were released from the G2-arrest at 6 h.

(A) Data in (A) are representative of several replicates, but samples were taken from a separate time course than those used for (B–D). (A) Rim4–3V5 SDS-resistant assemblies were analyzed by SDD-AGE (upper). Pgk1 SDS-PAGE is shown as a loading control (lower) (biological replicates > 5).

(B) Quantification of S2B. Rim4 protein is normalized to Pgk1 protein loading control (biological replicates = 4).

(C) Quantification of S2B. Clb3 protein (normalized to Pgk1 loading control) is corrected to *CLB3* mRNA (normalized to *rRNA* loading control) (biological replicates = 4).
(D) The images show Rim4–3V5 (anti-V5, red), tubulin (anti-tubulin, green) and DAPI (blue) in representative meiotic cells in metaphase I, anaphase I, metaphase II, and anaphase II. Scale bar, 2 mm. Shown are representative images from three biological replicates.
(E) Single-cell Rim4 levels in metaphase I (Met I), anaphase I (Ana I), metaphase II (Met II), and anaphase II (Ana II) were determined by anti-V5 immunofluorescence (IF) (n = 50 cells for each meiotic stage). Error bars indicate standard error of the mean. Statistical significance ($p < 0.05$ *; $p < 0.01$ **; $p < 0.001$ ***) was determined by Student's t test (biological replicates = 3).

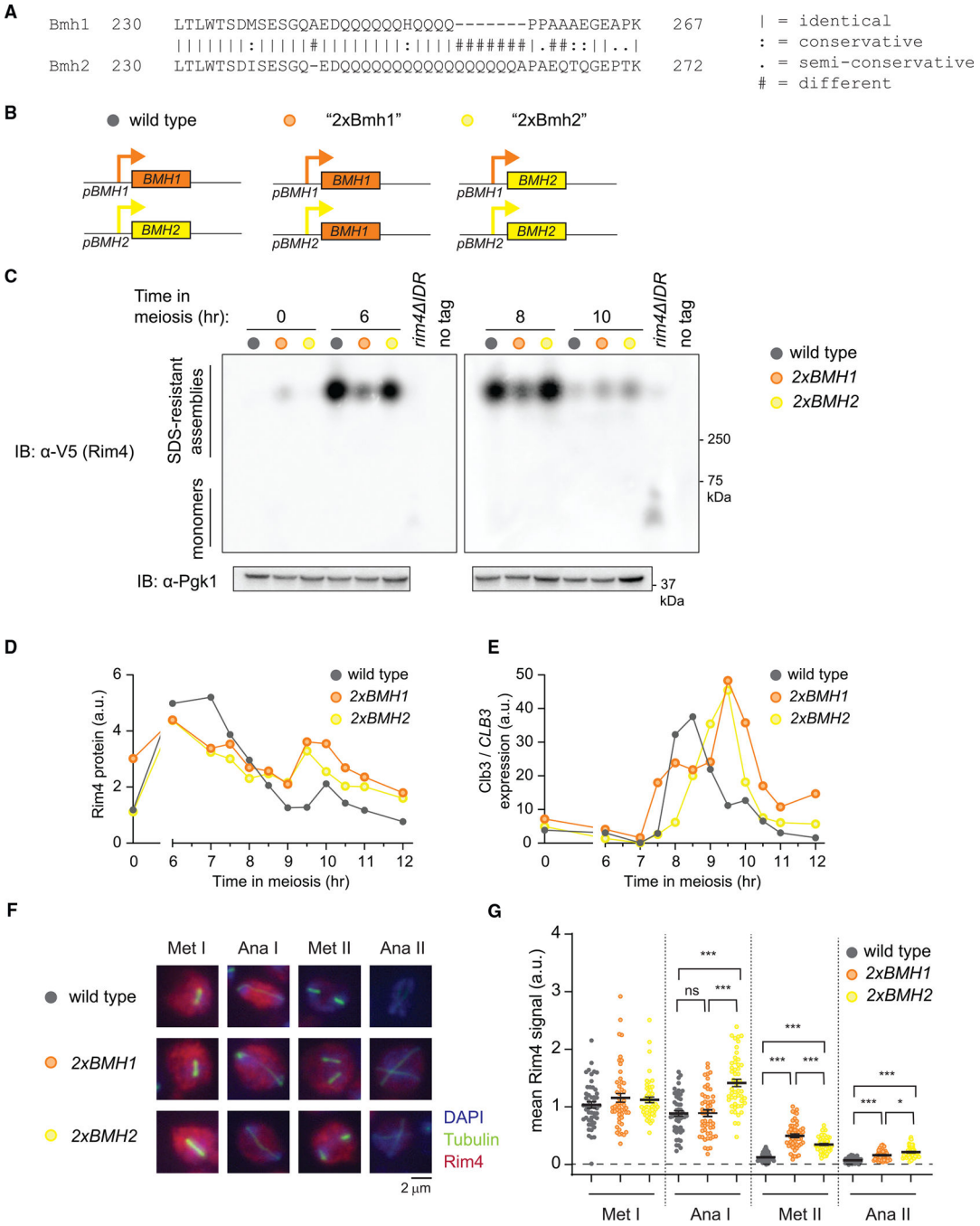

Figure 3. Bmh1 and Bmh2 play distinct roles in timely Rim4 clearance

(A) Sequence alignment of C termini of Bmh1 and Bmh2.

(B) Schematic of *BMH* promoters and coding sequences swapped in *2xBMH1* and *2xBMH2* cells.

(C–G) Strains harboring *NDT80-IN*, *RIM4–3V5*, *CLB3–3HA*, and either *BMH1; pBMH2-bmh2Δ::BMH1* (B2234, orange, *2xBMH1*), *pBMH1-bmh1Δ::BMH2; BMH2* (B2240, yellow, *2xBMH2*) or wild-type *BMH1; BMH2* (B48, gray) were induced to sporulate at 30°C. Cells were released from the G2 arrest at 6 h.

(C) Rim4–3V5 SDS-resistant assemblies were analyzed by SDD-AGE (upper). Pgk1 SDS-PAGE is shown as a loading control (lower) (biological replicates = 2).
(D) Quantification of S3E. Rim4 protein is normalized to Pgk1 protein loading control (biological replicates = 3).
(E) Quantification of S3E. Clb3 protein (normalized to Pgk1 loading control) is corrected to *CLB3* mRNA (normalized to *rRNA* loading control) (biological replicates = 3).
(F) The images show Rim4–3V5 protein (anti-V5, red), tubulin (anti-tubulin, green), and DAPI (blue) in representative meiotic cells in Met I, Ana I, Met II, and Ana II. Scale bar, 2 μm. Shown are representative images from three biological replicates.
(G) Single-cell Rim4 levels in Met I, Ana I, Met II, and Ana II were determined by IF (n = 50 cells for each meiotic stage). Error bars indicate standard error of the mean. Statistical significance ($p < 0.05$ *; $p < 0.01$ **; $p < 0.001$ ***) was determined by Student's t test (biological replicates = 3).

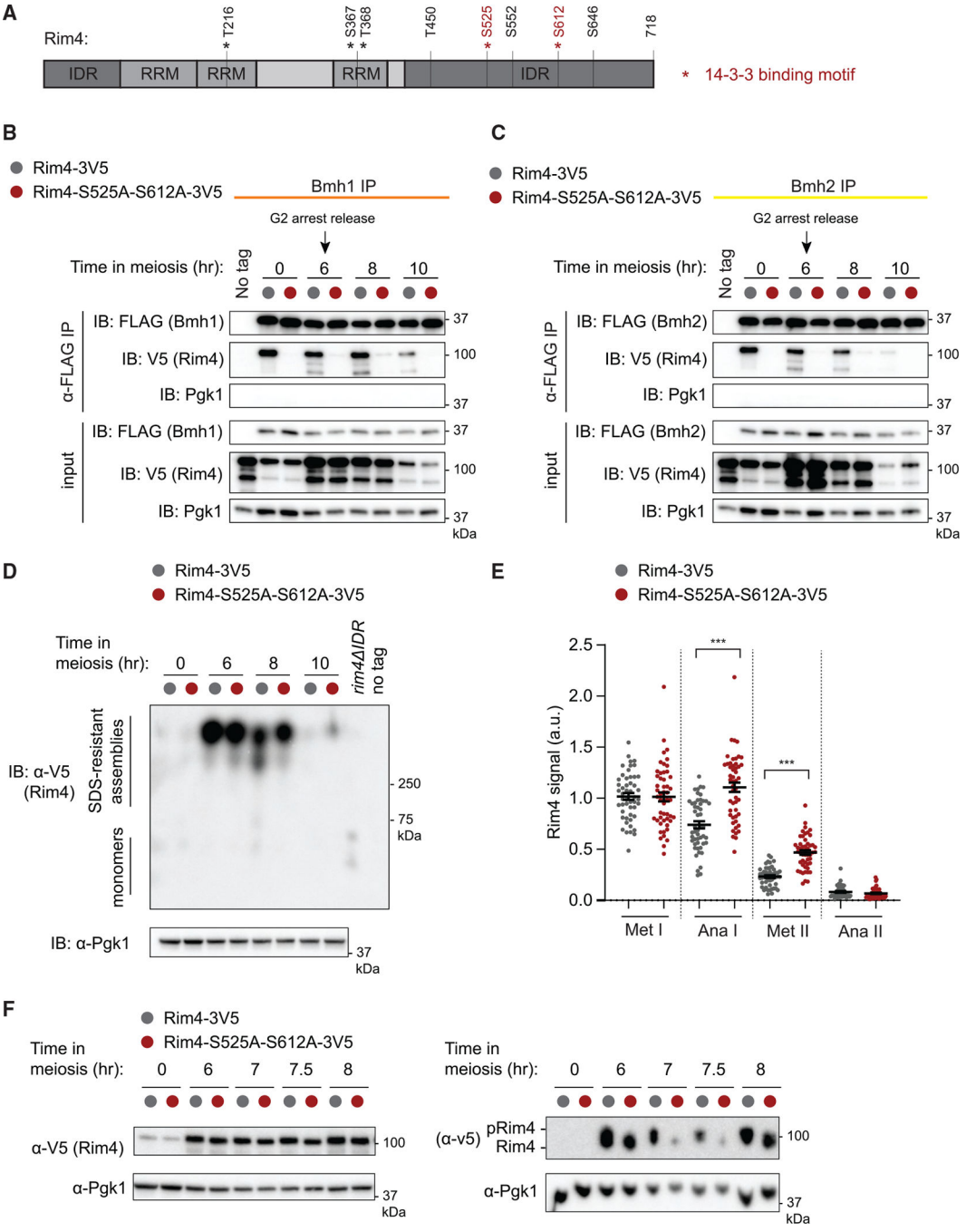

Figure 4. A priming phosphorylation is required for the interaction between Rim4 and Bmh proteins

(A) Diagram of Rim4. 14-3-3 consensus binding motifs are shown in red with an asterisk (Madeira et al., 2015). S612 in SK1 (strain used in this paper) is S607 in S288c strain used in the 14-3-3-Pred database.

(B) Strains harboring *NDT80-IN*, *BMH1-FLAG*, and either wild-type *RIM4–3V5* (B2169, gray), or *RIM4-S525A-S612A-3V5* (B3001, red) were induced to sporulate at 30°C. A strain harboring *NDT80-IN* and wild-type *RIM4–3V5* was used as a no FLAG tag control. Bmh1-FLAG was IPed from meiotic lysate at the indicated time points using anti-FLAG

agarose beads. Shown are Bmh1, Rim4, and Pgk1 (non-interacting control) protein levels by immunoblot in anti-FLAG IP and input samples (upper) (biological replicates = 2). (C–F) Strains harboring *NDT80-IN*, *BMH2-FLAG*, and either wild-type *RIM4–3V5* (B2170, gray) or *RIM4-S525A-S612A-3V5* (B3002, red) were induced to sporulate at 30°C. A strain harboring *NDT80-IN* and wild type *RIM4–3V5* was used as a no FLAG tag control. (C) Bmh2-FLAG was IPed from meiotic lysate at the indicated time points using anti-FLAG agarose beads. Shown are Bmh2, Rim4, and Pgk1 (non-interacting control) protein levels by immunoblot in anti-FLAG IP and input samples (upper) (biological replicates = 2). (D) Rim4–3V5 SDS-resistant assemblies were analyzed by SDD-AGE (upper). Pgk1 SDS-PAGE is shown as a loading control (lower) (biological replicates = 2). (E) Single-cell Rim4 levels in Met I, Ana I, Met II, and Ana II were determined by IF (n = 50 cells for each meiotic stage except ana I wild type where n = 15). Error bars indicate standard error of the mean. Statistical significance ($p < 0.05$ *; $p < 0.01$ **; $p < 0.001$ ***) was determined by Student's t test. Shown are representative images of 2 biological replicates. (F) SDS-PAGE (left) and phos-tag SDS-PAGE (right) comparing electrophoretic migration of Rim4 and Rim4-S525A-S612A-3V5. Shown are Rim4 and Pgk1 protein levels by immunoblot. This experiment is n = 1.

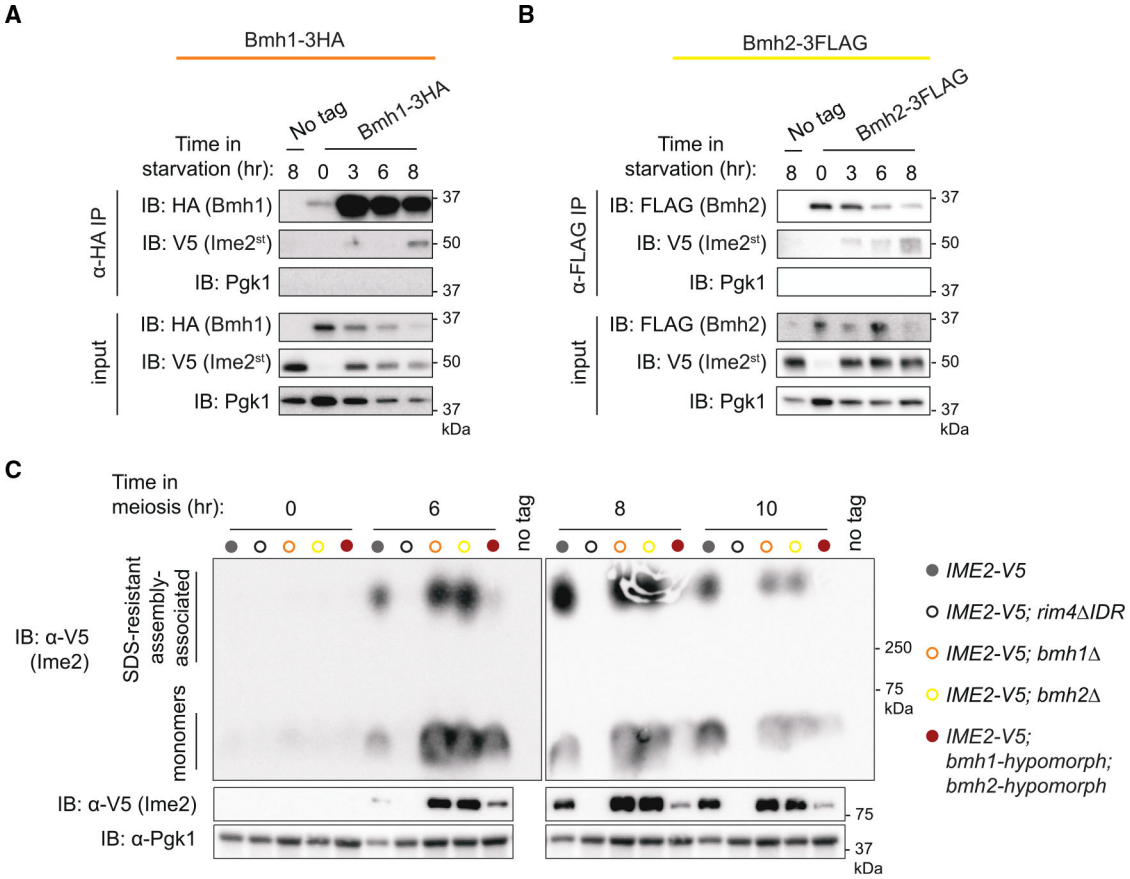

Figure 5. Bmh1 and Bmh2 are important for the interaction between Rim4 and Ime2

(A and B) Strains harboring *NDT80-IN*, *IME2st-3V5*, and either untagged *BMH1/2* (B1686) or *BMH1–3HA* and *BMH2–3FLAG* (B1683) were induced to sporulate at 30°C. Cells were held in G2 arrest and samples were collected at the indicated hours in sporulation medium. (A) Bmh1–3HA was IPed from meiotic lysate using anti-HA agarose beads. Shown are Bmh1, Ime2st, and Pgk1 (non-interacting control) protein levels by immunoblot in IP and input samples (biological replicates = 2). (B) Bmh2–3FLAG was IPed from meiotic lysate using anti-FLAG agarose beads. Shown are Bmh2, Ime2st, and Pgk1 (non-interacting control) protein levels by immunoblot in IP and input samples (biological replicates = 2). (C) Strains harboring *NDT80-IN*, *IME2-V5*, and either wild-type *BMH1/2* (B1680, gray), *rim4ΔIDR-3FLAG* (B236, black empty circle), *bmh1*Δ (B2541, orange empty circle), *bmh2*Δ (B2544 yellow, empty circle), or double *bmh* hypomorphic alleles (B2547, *BMH1-AID* and *BMH2-AID*, B2547, red) were induced to sporulate at 30°C. Ime2 association with SDS-resistant assemblies was analyzed by SDD-AGE (upper). Ime2–3V5 and Pgk1 (loading control) protein levels are determined by SDS-PAGE (lower) (biological replicates = 3).

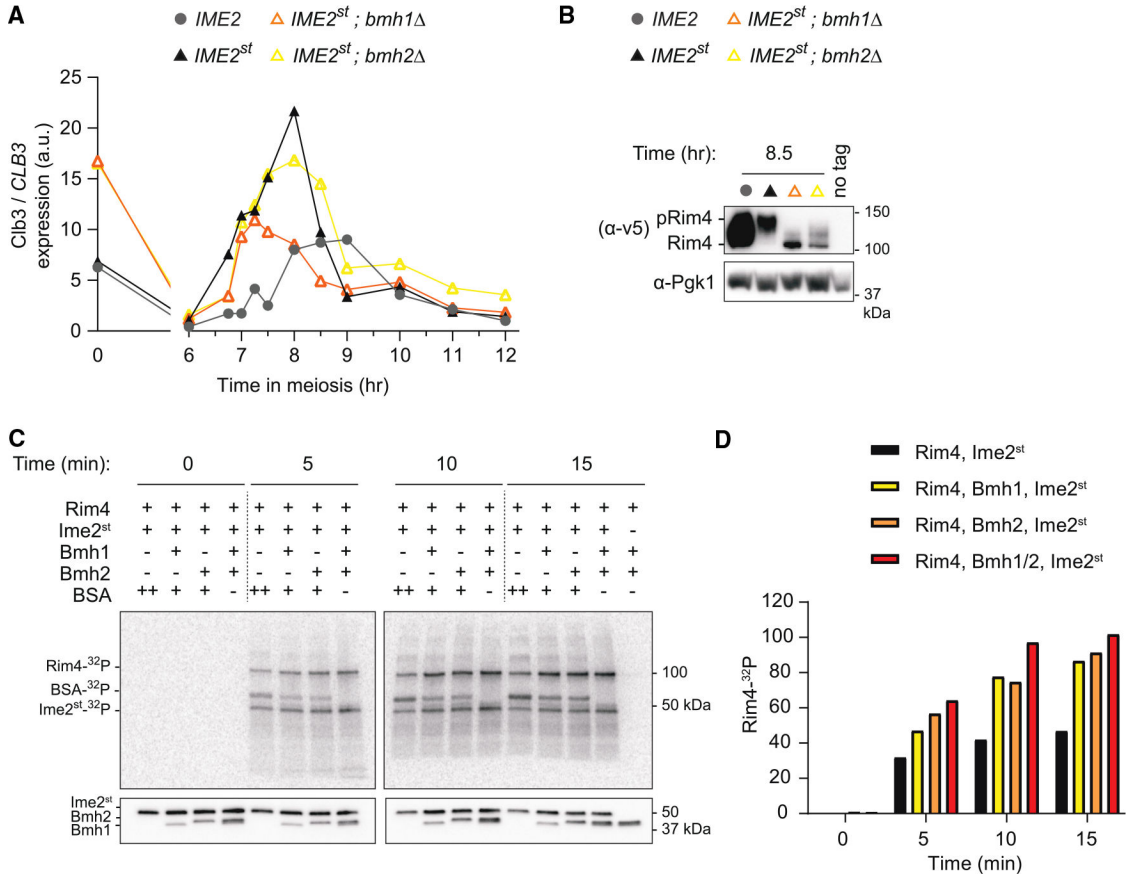

Figure 6. Bmh1 and Bmh2 facilitate phosphorylation of Rim4 by Ime2

(A and B) Strains harboring *NDT80-IN*, *RIM4–3V5*, *CLB3–3HA*, and either *IME2–3V5* and wild-type *BMH1/2* (B79, gray circle) or *IME2*st*-3V5* with wild-type *BMH1/2* (B82, black triangle), *bmh1*Δ (B1462, orange triangle), or *bmh2*Δ (B1463, yellow triangle) were induced to sporulate at 30°C. Cells were released from G2 arrest and samples were collected at the indicated times. (A) Quantification of S6. Clb3 protein (normalized to Pgk1 loading control) is corrected to *CLB3* mRNA (normalized to *rRNA* loading control) (biological replicates = 2). (B) Rim4–3V5, pRim4–3V5, and Pgk1 (loading control) protein are determined by immunoblot of a phos-tag SDS-PAGE gel (biological replicates = 4). (C) Determination of Ime2st kinase activity in the presence and absence of Bmh proteins. Each kinase reaction contains a combination of assembled Rim4–3C, Ime2st-3FLAG, Bmh1–3FLAG, and/or Bmh2–3FLAG as indicated. BSA is used as a control (equivalent w/v) for molecular crowding in reactions that do not include Bmh1, Bmh2, or both. Incorporation of radiolabeled ATP was assessed at the indicated times (upper). Ime2st, Bmh1, and Bmh2 protein levels are shown by anti-FLAG immunoblot (lower) (biological replicates = 3).

(D) Quantification of Rim4–^{32}P shown in (C).

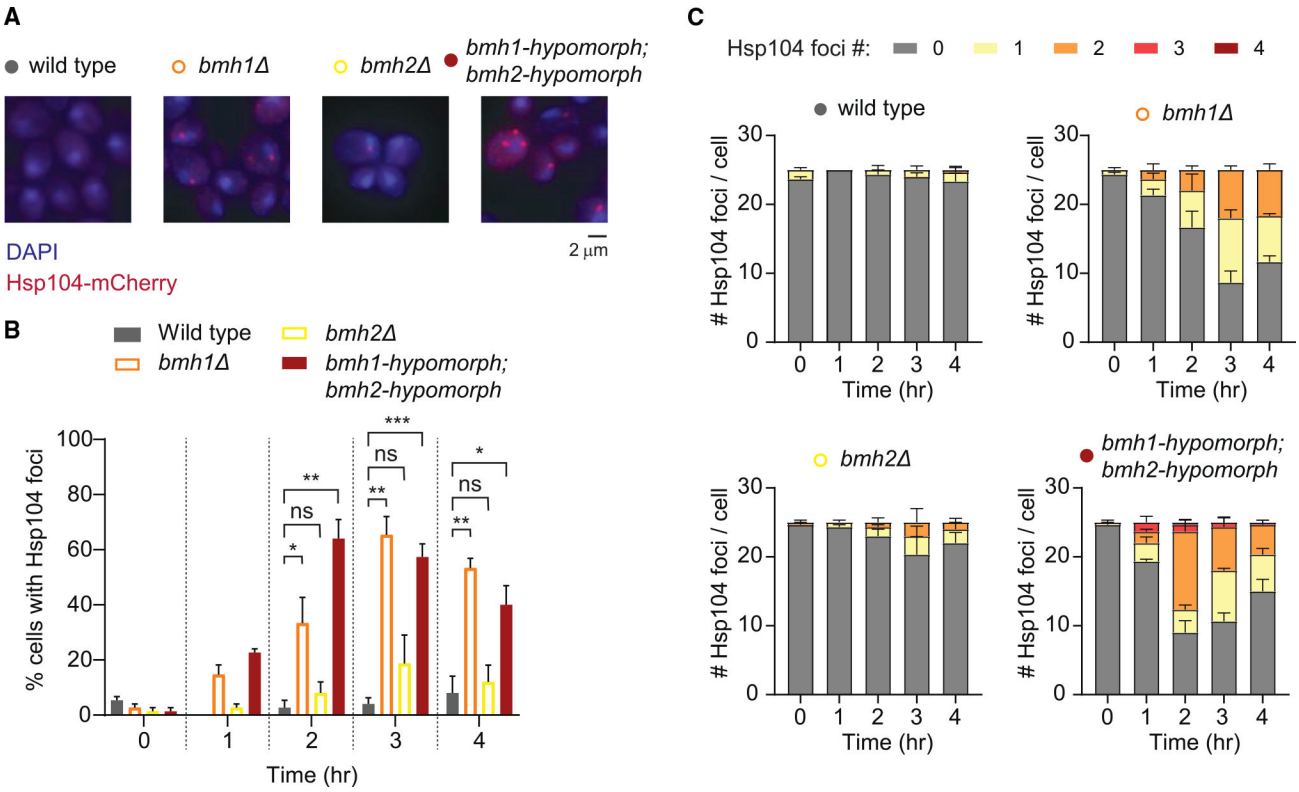

Figure 7. Bmh1 and Bmh2 are important for maintaining protein aggregate homeostasis

Haploid strains harboring *HSP104-mCherry* and either wild-type *BMH1/2* (A35843, gray circle), *bmh1*Δ (B2858, orange empty circle), *bmh2*Δ (B2860, yellow empty circle), or *BMH1-AID*; *BMH2-AID* (B2862, red circle) were resuspended in YPD at OD_{600} = 0.2 and allowed to grow at 30°C.

(A) The images show Hsp104-mCherry (red) and DAPI (blue) in representative mitotic cells at t = 3 h after resuspension in YPD. Scale bar, 2 μm. Shown are representative images of three biological replicates.

(B) Single-cell Hsp104-mCherry levels were determined by fluorescence microscopy (n = 25 cells for each time point). Foci were determined by measuring signal intensity in cell area with highest signal and lowest signal. Cells were classified as having a focus if the highest intensity measurement was 1.5 times the lowest internal signal. Error bars indicate standard error of the mean. Statistical significance ($p < 0.05$ *; $p < 0.01$ **; $p < 0.001$ ***) was determined by Student's t test (biological replicates = 3).

(C) Number of foci per cell was determined (n = 25 cells for each time point). Error bars indicate standard error of the mean (biological replicates = 3).

KEY RESOURCES TABLE

REAGENT or RESOURCE	SOURCE	IDENTIFIER
Antibodies		
α-HA.11 Clone:16B12 (mouse)	BioLegend	Cat# 901514
α-Pgk1 (Phosphoglycerate Kinase monoclonal) (mouse)	Novex (Life Technologies)	Part# 459250
α-v5 monoclonal (mouse)	Invitrogen	Cat# 46-0705
α-FLAG (rabbit)	Sigma-Aldrich	Cat# F7425
α-14-3-3 (rabbit)	(Gelperin et al., 1995)	N/A
α-mouse HRP-conjugated secondary	GE Healthcare	Cat# NA931-1ML
α-rabbit HRP-conjugated secondary	GE Healthcare	Cat# NA934V
α-V5-coupled agarose	Sigma-Aldrich	Cat# A7345-1mL
α-FLAG M2 affinity gel	Sigma-Aldrich	Cat# F1804
α-HA-coupled agarose	Sigma-Aldrich	Cat# B9183
α-tubulin alpha (rat)	Bio-Rad	Cat# MCA77G
α-rat-FITC	Invitrogen	Cat# 31629
α-mouse-Cy5	Thermo Scientific	Cat# A10524
Chemicals, peptides, and recombinant proteins		
Halt Protease Inhibitor	ThermoFisher	Cat# 1861279
ProlongGold anti-fade reagent w/ DAPI	Invitrogen	Cat# P36935
β-Estradiol	Sigma-Aldrich	Cat# E8875
Acid-washed glass beads, 425-600 mm	Sigma-Aldrich	Cat# G8772-500G
0.5 mm dia Zirconia/silica beads	BioSpec Products	Cat# 11079105Z
Hybond-N+ membrane	GE Healthcare	Prod# RPN203B
10% Criterion TGX Precast Midi Protein Gel, 26 well, 15 mL	Bio-Rad	Cat# 5671035
FLAG peptide	APExBIO	Cat# A6001
SuperSep™ Phos-tag™ (50mmol/L), 7.5%, 17well, 83 3 100 × 3.9mm	FUJIFILM Wako Pure Chemical Corporation	Prod# 198-17981
Trans-blot turbo transfer kits (Nitrocellulose)	Bio-Rad	Cat# 1704271
Illustra Probequant Columns	GE Healthcare	Prod# 28903408
Critical commercial assays		
Amersham MegaPrime DNA Labeling Kit	GE Healthcare	Prod# RPN1604
Deposited data		
Rim4 immunopurification and quantitative mass spectrometry	this paper	Accession# MSV000089188
Experimental models: Organisms/strains		
All lab strains are S. cerevisiae, of SK1 background (see Table S1)	(Kane and Roth, 1974)	ATCC: 204,722
Oligonucleotides		

REAGENT or RESOURCE	SOURCE	IDENTIFIER
FW primer for CLB3 Northern probe: 5'-AGCATAAGTAAGCCAAAAGTCGC-3′	(Carlile and Amon, 2008)	N/A
RV primer for CLB3 Northern probe: 5'-CTAATGCTATCCACTTCGCTACG-3′	(Carlile and Amon, 2008)	N/A
Recombinant DNA		
Construct: *ura3::pGPD-GAL4(848).ER::URA3*	(Benjamin et al., 2003)	N/A
Construct: *CLB3-3HA:kanMX6*	(Carlile and Amon, 2008)	N/A
Construct: *RIM4-3V5::His3MX6*	(Berchowitz et al., 2013)	N/A
Construct: *RIM4Δ267-3V5::His3MX6*	(Berchowitz et al., 2015)	N/A
Construct: *BMH1-3FLAG::kanMX6*	this paper	N/A
Construct: *BMH2-3FLAG::kanMX6*	this paper	N/A
Construct: *BMH1Δ::kanMX6*	this paper	N/A
Construct: *BMH2Δ::His3MX6*	this paper	N/A
Construct: *RIM4-646A-3V5::kanMX6*	(Carpenter et al., 2018)	N/A
Construct: *RIM4-450-552A-3V5::kanMX6*	(Carpenter et al., 2018)	N/A
Construct: *RIM4-552A-3V5::kanMX6*	(Carpenter et al., 2018)	N/A
Construct: *RIM4-450A-3V5::kanMX6*	(Carpenter et al., 2018)	N/A
Construct: *pBMH2-BMH1::kanMX6*	this paper	N/A
Construct: *pBMH1-BMH2::kanMX6*	this paper	N/A
Construct: *IME2st-3V5::His3MX6*	(Carpenter et al., 2018)	N/A
Construct: *BMH1-3HA::His3MX6*	this paper	N/A
Construct: *IME2-3V5::His3MX6*	(Carpenter et al., 2018)	N/A
Construct: *RIM4Δ271-3V5::His3MX6*	(Berchowitz et al., 2015)	N/A
Construct: *his3::pRIM4-OsTIR1::His3MX6*	(Sawyer et al., 2019)	N/A
Construct: *BMH1-AID-6FLAG::HYGR*	this paper	N/A
Construct: *BMH2-AID-9myc::kanMX6*	this paper	N/A
Construct: *RIM4-3FLAG::kanMX6*	(Carpenter et al., 2018)	N/A
Construct: *HSP104-mCherry-NAT*	this paper	N/A
Plasmid: pFA6a-His3MX6	(Longtine et al., 1998)	https://www.addgene.org/41596/
Plasmid: pFA6a-kanMX6	(Longtine et al., 1998)	https://www.addgene.org/39296/
Plasmid: pFA6a-3HA-His3MX6	(Longtine et al., 1998)	https://www.addgene.org/41600/
Plasmid: p3FLAG-KanMX	(Gelbart et al., 2001)	N/A
Plasmid: pHyg-AID*-6FLAG	(Morawska and Ulrich, 2013)	https://www.addgene.org/99519/
Plasmid: pHyg-AID*-9myc	(Morawska and Ulrich, 2013)	https://www.addgene.org/99518/
Plasmid: pFA6a-mCherry-natMX6	(Snaith et al., 2005)	N/A
Software and algorithms		
Fiji software	(Schindelin et al., 2012)	https://fiji.sc/
Other		
DeltaVision Elite Microcope	GE Healthcare	Prod #: 29065728

REAGENT or RESOURCE	SOURCE	IDENTIFIER
FastPrep-24	MP biomedicals	Cat# 6004500
Trans-Blot Turbo Transfer System	Bio-Rad	Cat# 1704150